Geochemistry, Geophysics, Geosystems®

AGU ADVANCING EARTH AND SPACE SCIENCES

RESEARCH ARTICLE
10.1029/2024GC011840

Micro-Scale Characterization of Marine Sediment Structures: The Potential and Challenges of X-Ray µCT Imaging

R. Gatter[1,2], G. Bartzke[1], B. N. Madhusudhan[3], S. Ahmed[4], M. Clare[5], M. Vardy[6], and K. Huhn[1]

[1]MARUM – Center for Marine Environmental Sciences, University of Bremen, Bremen, Germany, [2]Faculty of Geosciences, University of Bremen, Bremen, Germany, [3]Faculty of Engineering and Physical Sciences, University of Southampton, Southampton, UK, [4]Diamond Light Source, Didcot, UK, [5]Ocean BioGeoscience Research Group, National Oceanography Centre, Southampton, UK, [6]SAND Geophysics Ltd, Southampton, UK

Key Points:

- Synchrotron X-ray µCT reveals small-scale heterogeneity in sediment structures that is missed by standard geotechnical tests
- Pore space distribution in natural marine sediments is highly spatially variable and affects sediment structures on a sub-millimeter scale
- Compositional and structural differences in coarse- and fine-grained marine sediments reveal a dependency on the sedimentation regime

Supporting Information:

Supporting Information may be found in the online version of this article.

Correspondence to:

R. Gatter,
rgatter@marum.de

Citation:

Gatter, R., Bartzke, G., Madhusudhan, B. N., Ahmed, S., Clare, M., Vardy, M., & Huhn, K. (2025). Micro-scale characterization of marine sediment structures: The potential and challenges of X-ray µCT imaging. *Geochemistry, Geophysics, Geosystems*, *26*, e2024GC011840. https://doi.org/10.1029/2024GC011840

Received 21 AUG 2024
Accepted 9 MAR 2025

Author Contributions:

Conceptualization: R. Gatter, G. Bartzke, M. Clare, K. Huhn
Data curation: R. Gatter, B. N. Madhusudhan
Formal analysis: R. Gatter
Funding acquisition: K. Huhn
Investigation: R. Gatter
Methodology: R. Gatter, B. N. Madhusudhan, S. Ahmed, M. Vardy
Project administration: B. N. Madhusudhan, M. Vardy, K. Huhn

Abstract Natural marine sediments are heterogeneous with respect to sediment-physical properties, and have a wide range in composition and structures. For many years, sediment-physical characterization has relied primarily on laboratory experiments. However, the investigation of small-(grain-)scale sedimentary structures, which appear to control many sediment (re-)depositional and emplacement mechanisms, requires new analytical methods. Here, we test high-resolution X-ray synchrotron micro-tomography (µCT) to qualitatively and quantitatively investigate structural differences, in 3D, between two lithological end-member types of marine sediments: a coarse-grained, sandy sediment and a fine-grained, silty-clay sediment. Our results show clear compositional and structural differences between the two end-members, as well as between samples taken from the same lithological unit. These differences can be attributed partly to different sediment types, that is, coarse-versus fine-grained sediments, but also reveal a dependency on the sedimentation regime. We find that pore space distribution is highly spatially variable, even down to a sub-millimeter scale. Such high variability in porosity would be missed by standard geotechnical experiments, which only provide information averaged over far larger sediment samples. The identification of small-(grain-)scale changes in pore space, however, directly impacts sediment properties such as permeability, which in turn is crucial for the understanding of geological processes such as fluid flow and storage capacity of sediments and assessing hazards such as the preconditioning of submerged slopes to collapse. Our results therefore demonstrate the potential of µCT to investigate the internal structure of natural sediments, obtaining information that is not resolved or lost in data acquired through other analytical methods.

Plain Language Summary Natural sediments are very diverse with a wide range of structures, including differences in grain and pore size, shape and arrangement. Unraveling these differences is key to understanding important geological processes, which are deduced from sediment characterization. A major problem when investigating sediment, however, is typically related to the limited resolution of standard laboratory techniques. Most techniques do not allow the investigation of sediment structures on a micro-grain-scale. In this study, we investigate the size, shape and distribution of grains and related pore spaces in sediment samples of natural fine- and coarse-grained ocean-floor sediments to determine structural differences caused by the environmental setting. We quantify three-dimensional geometric and material information for the pore spaces using high-resolution 3-D X-ray synchrotron micro-Tomography images of the sediment samples. We found that pore space distribution is highly variable, even down to a sub-millimeter scale, in both 2-D and 3-D. The images also reveal that pore spaces not only vary between fine- and coarse-grained samples, but also throughout individual sediment samples. Therefore, our results demonstrate the high potential of high-resolution imaging to investigate natural sediment structures, and to gain deeper insights into various sediment transport and depositional processes in the marine and aquatic realm.

1. Introduction

Technological progress, especially during the last century, has resulted in an explosion of knowledge in geosciences. This progress has, in part, radically transformed our view and understanding of the geoscientific processes that shape our Earth. The ocean floor is comparatively less well explored despite covering approximately 70% of the Earth's surface (Eakins & Sharman, 2010). The vast majority of the ocean floor is virtually unmapped (e.g., Mayer et al., 2018), with about 26.1% of the global ocean mapped at a resolution of 100 m or better (www.

Software: R. Gatter, B. N. Madhusudhan, S. Ahmed
Supervision: G. Bartzke, B. N. Madhusudhan, M. Clare, K. Huhn
Validation: R. Gatter
Visualization: R. Gatter, G. Bartzke, K. Huhn
Writing – original draft: R. Gatter, K. Huhn
Writing – review & editing: G. Bartzke, B. N. Madhusudhan, M. Clare, M. Vardy

seabed2030.org). In addition, only a small portion of the ocean floor has been geophysically surveyed, revealing information about the internal structure of the shallow and deeper subsurface (e.g., Favali & Beranzoli, 2006). Such information, however, is key to understanding the geological processes that act on and shape the seafloor. Filling remaining knowledge gaps is a prerequisite to understanding the wide spectrum of geological processes and thereby coping with the ever increasing need for future sustainable usage strategies of marine resources, such as spatial planning strategies, the construction and operation of offshore infrastructure, the designation of marine protected areas, the implementation of environmental monitoring programmes, and the assessment of natural hazards that initiate in the ocean (e.g., Brown et al., 2012; Leon et al., 2020; Randolph et al., 2011; Rudolph et al., 2020; Santos et al., 2019; Sauvin et al., 2022; St. Martin & Hall-Arber, 2008; Vardy, 2022).

Natural marine seafloor sediments can be highly heterogeneous. Even basic physical properties, such as density, porosity and/or permeability, can vary strongly even on very small scales, both laterally and vertically (e.g., Bennet et al., 1990; Daigle, 2014; Li et al., 2020). In turn, this variability can create significant differences in material strength and its behavior following initial deposition and under external loading (e.g., Bartetzko & Kopf, 2007; Chen et al., 2020; Hassan et al., 1998; Kim et al., 2007; Lee et al., 2011; Lv et al., 2021; Wetzel, 1990). Associated therewith is an impact on sediment stability, its transport behavior, or the effects on migrating fluids through the subsurface, to name just a few aspects of scientific and commercial interest. Hence, precise physical characterization is crucial as we rely on this information to interpret and understand the underlying geological processes that cannot be observed directly.

Porosity and permeability are two of the most important material properties to investigate fluid flow through sediments and predict their post-depositional behavior (e.g., Maltman, 1994; Maltman & Bolton, 2003). However, how precisely porosity and permeability vary across sediments often remains unclear. Physical samples, particularly sediment cores, are a fundamental resource from which to determine sediment composition and physical properties. For many years, physical parameter characterization relied on core-logging and geotechnical laboratory tests that yield directly or indirectly required sediment properties (e.g., Badhani et al., 2020; Freeman & Schüttenhelm, 1990; Rothwell & Rack, 2006; Sammartini et al., 2021). Small, sub-centimeter- to sub-millimeter-scale variations in sediment properties, in particular geotechnical properties, however, are difficult to resolve with standard core-analytical methods. Standard core-logging techniques, such as multi-sensor core logging, can only provide fractional porosity estimates that are typically limited to down-core resolutions of centimeters to millimeters (Rothwell & Rack, 2006). Although geotechnical tests can provide more accurate porosity estimates and further information such as permeability estimates, these tests require large (several centimeters), undisturbed sediment samples. Such samples are relatively scarce, and even if adequate sample material is available, the amount of information they can provide is limited to measurements averaged over the entire sample and is usually only unidirectional; for example, the determination of relative permeability is usually conducted with flow in only one direction (often vertical, along the axis of the core) using whole-round cases. Hence, although existing conventional analytical methods provide valuable insights into many sediment-physical aspects of marine sediments, there is still a clear lack of knowledge regarding micro-(grain-)scaled material heterogeneities.

In many cases, visual sediment core descriptions reveal no observable downcore changes in sediment composition or texture, despite apparent significant lateral and vertical variations in sediment-physical properties (e.g., Kim et al., 2007; Riedel et al., 2020; Sawyer et al., 1997). Recent studies have explained such variations with differences in small-(grain-)scale sediment texture and structure (e.g., Gatter et al., 2021; Kim et al., 2007; Lee et al., 2011; Lu & Li, 2003). Marine sediments are composed of grains and particles of various mineralogy and shapes that govern complex micro-scale sediment fabrics (e.g., Cornard et al., 2023; Lee et al., 2011). The arrangement of and interactions between different sediment components place critical constraints on physical processes, such as fluid flow that occur in subseafloor environments and thereby, play an important role in controlling geological processes (e.g., Koltermann & Gorelick, 1996; Mitra et al., 2024; Santos et al., 2012).

Previous studies have highlighted the relation between sediment microstructures and geotechnical properties (e.g., Kim et al., 2007; Lee et al., 2011). To investigate sediment microstructures, various methods have been used, such as X-ray diffraction (XRD; e.g., Forsberg & Locat, 2005; Lee et al., 2011), mercury injection porosimetry (MIP; Hattab et al., 2013), scanning electron microscopy (SEM; Kim et al., 2007; Hattab et al., 2013), transmission electron microscopy (TEM; Ransom et al., 1999), and nuclear magnetic resonance (NMR; Fox et al., 2018). Although each has its own advantages, the effectiveness of these methods in identifying

and characterizing microstructures is limited due to their often inversive nature and because these methods can generally only provide information in 2D. The 2D nature of the measurements may in turn cause significant errors in 3D structural reconstructions and interpretations. The investigation of micro-(grain-)scale sedimentary structures, in 3D, therefore requires alternative analytical methods and technologies to close important knowledge gaps.

One technique that has shown great potential for the application in geosciences is X-ray Computed Tomography (CT; e.g., Mees et al., 2003; Cnudde & Boone, 2013). High-resolution X-ray micro-Tomography (μCT) techniques, in particular, have found increased application for the investigation of micro-scale sediment structures (e.g., Bendle et al., 2015; Cornard et al., 2023; Johnson et al., 2019; Sleutel et al., 2008; Wildenschild & Sheppard, 2013). Similar to conventional medical CT, μCT enables the visualization of the scanned material in 3D, but at much higher resolutions (e.g., Cnudde & Boone, 2013). Despite the increasing recognition and application of CT systems in geosciences, the technique is also approaching its physical limitations (e.g., Cnudde & Boone, 2013; Sasov et al., 2008; Withers et al., 2021) and only a few studies have tested the potential of high-resolution (sub-micrometer resolution) μCT to investigate marine sediment structures.

1.1. Aims and Objectives

In this study, we discuss the application of X-ray μCT to investigate natural marine sediments, in 3D, and test its potential to characterize complex sediment structures on a micro-(grain-)scale level. We give a brief review of (μ) CT systems that find application in geosciences, followed by a detailed μCT analysis of two typical marine lithological endmembers.

To demonstrate the advantages and disadvantages of μCT imaging for structural investigations of marine sediments, a total of four sediment samples were taken from two exemplary sediment cores that sampled marine sediments from different geological environments (see, 3.1 Sample material). Two samples (D1 and D2) were taken from a fining-upwards sand layer and used as coarse-grained marine sediment end-members. Another two samples (D3 and D4) were taken from a homogeneous silty-clay layer and used as fine-grained marine sediment end-member. High-resolution μCT was used to visualize, and qualitatively and quantitatively investigate structural differences, in particular porosity and pore space variability, between the samples. The comparison of these four samples, thereby, aims to investigate (a) structural differences between at least two lithological endmembers of marine sediments and (b) structural variability within the two sampled lithological units.

Specifically, we tackle the following overarching questions. First, what information can μCT provide that is currently missing from standard sediment core analyses? Based on novel high-resolution 3D μCT data of marine sediments, we discuss the potential of μCT imaging for sedimentological investigations and characterization of structural properties. In particular, we focus on the quantification and qualitative investigation of pore space evolution throughout two lithological units, a fining-upwards sand (D1 and D2) and an apparently homogeneous (on the basis of visual assessment and standard geotechnical characterization) silty-clay (D3 and D4). Second, what are the current limitations of μCT analyses in particular with regard to the investigation of marine sediments? Although CT imaging has been used for a long time, the method, in particular high-resolution μCT imaging, still finds limited application in marine geosciences. We discuss and evaluate potential reasons and point out current analytical limitations before outlining potential ways to overcome these limitations.

2. X-Ray Computed Tomography (CT)

X-ray CT is a non-invasive imaging technique that enables the visualization of the internal structure of scanned objects and materials at scales ranging from meters to only tens of nanometers (e.g., Hampel, 2022; Ketcham & Carlson, 2001; Mees et al., 2003; Withers et al., 2021). This method uses X-rays to obtain a series of two-dimensional (2D) radiographs of the scanned object from various positions during step-wise rotation around a central axis. These radiographs are subsequently used to create a stack of parallel cross-sectional slices of the object, which in turn provide a digital three-dimensional (3D) greyscale representation of the internal structure of the object (e.g., Mees et al., 2003; Withers et al., 2021). CT imaging enables discrimination between materials with different X-ray attenuation, which is a function of the material's composition (effective atomic number) and density (e.g., Cnudde & Boone, 2013). X-ray attenuation is described by the Lambert-Beer law (e.g., Cnudde & Boone, 2013; Phillips & Lannutti, 1997) that states that X-rays are attenuated as a function of the material they are

propagating through, and can be used to visualize subtle changes in sediment composition (e.g., Goldfinger et al., 2012; Van Daele et al., 2014; van der Bilt et al., 2021).

Although various configurations exist, the basic components of X-ray scanners comprise an X-ray source, a detector and a rotation system. One important quality aspect is related to the energy spectrum produced by different X-ray sources (e.g., Orhan & Büyüksungur, 2020). Usually X-rays are polychromatic with a wide range of energy (e.g., Chung et al., 2019; Mees et al., 2003). This causes artefacts in the CT image due to the stronger attenuation of X-rays with low energies. To avoid such artefacts, monochromatic X-ray beams are desirable (e.g., Mees et al., 2003). Conventional medical or industrial CT systems, with typical spatial resolutions in the (sub-) millimeter range (voxel sizes ≥100 μm), can be used for large core scanning and dual energy scanning for chemical analysis of core samples (e.g., Withers et al., 2021). Despite several limiting factors (e.g., Cnudde & Boone, 2013; Sasov et al., 2008; Withers et al., 2021), the method has been used successfully to identify sediment core disturbances and for the evaluation of core quality (e.g., Orsi et al., 1994; Tonai et al., 2019), to study bioturbation and ichnofabrics in sediment cores (e.g., Dorador et al., 2020; Rodríguez-Tovar et al., 2018), to examine the presence, abundance and dissociation of gas hydrates in sediments (e.g., Kneafsey & Moridis, 2014; Waite et al., 2008), for turbidite and palaeoflow reconstruction (Howarth et al., 2021; Van Daele et al., 2014), or to characterize contourite deposits (Vandorpe et al., 2019) among others. Thus, CT scanning has become part of routine core analyses, enabling the investigation of surface as well as internal features, including bedding, sedimentary structures and deformations, or core disturbances.

To properly characterize features of interest (e.g., shape or volume), the *voxel* size (cubic volume elements that make up 3D images) needs to be significantly smaller than the size of the expected features (e.g., Withers et al., 2021). High resolution can only be obtained for small samples, for example, <2 mm diameter samples for a 5 μm resolution in CT scans, as resolution is a function of object distance from the scanner (e.g., Mees et al., 2003).

Micro-tomography or μCT imaging is unique in the sense that it allows the 3D visualization of the internal structure of the scanned material at a (sub-)micrometer resolution (voxel sizes ≥1 μm), while nano-tomography (nanoCT) refers to nanometer resolutions (down to voxel sizes around 10 nm). Such resolutions allow not only the recognition of subtle compositional changes, but also changes in sediment (pore) structure (e.g., Cnudde & Boone, 2013; Withers et al., 2021). Synchrotron X-rays are often preferred to laboratory-generated X-rays, because they offer high resolution scans within only a few minutes, better signal-to-noise ratio, and avoid beam hardening artefacts. Certain synchrotron facilities also carry out phase contrast imaging based on grating interferometry (Weitkamp et al., 2005), which can be used to detect boundaries between phases with similar X-ray absorption and contrast between different phases. This information can be used to infer the mineralogy of sediments from the index of refraction during reconstruction and visual observation (e.g., Wang & Miller, 2020).

3. Material and Methods

3.1. Sample Material

This study compiles qualitative and quantitative structural information of two typical marine lithologies: (a) a coarse-grained sandy and (b) a fine-grained silty clay sediments. In total, four sediment samples (D1–D4) were scanned and analyzed in terms of their structural and compositional characteristics by means of high-resolution 3D X-ray synchrotron micro-Tomography (μCT).

Two cylindrical samples (D1 and D2) were taken from the same lithological unit, a fining upwards sand, only 9 cm apart, at 2.95 m below seafloor (mbsf) and 3.04 mbsf of a sediment core that recovered fjordic sediments near the village of Finneidfjord (Norway) (Figure 1a; core GS10-163-02PC; Vanneste et al., 2011; L'Heureux et al., 2012). The samples were taken from the finer-grained upper (D1) and coarser-grained lower (D2) parts of a prominent sandy sediment layer that stratigraphically correlates with a well-defined regional event bed and was previously identified as a turbidite or sediment flow deposit (L'Heureux et al., 2012; Vardy et al., 2012). Another two cylindrical samples (D3 and D4) were taken at 9.18 mbsf and 9.25 mbsf (7 cm apart) of a sediment core that recovered marine sediments from the Faroe-Shetland Channel, offshore Northern Scotland (UK), respectively (Figure 1b; 64PE391-04; Gatter et al., 2020). Although the core recovered sediments from inside a landslide area (AFEN Slide Figure 1), the sampled lithological unit lies below the identified failure plane of the landslide and is therefore considered undisturbed (Gatter et al., 2020; Wilson et al., 2004). Both samples (D3 and D4) were taken

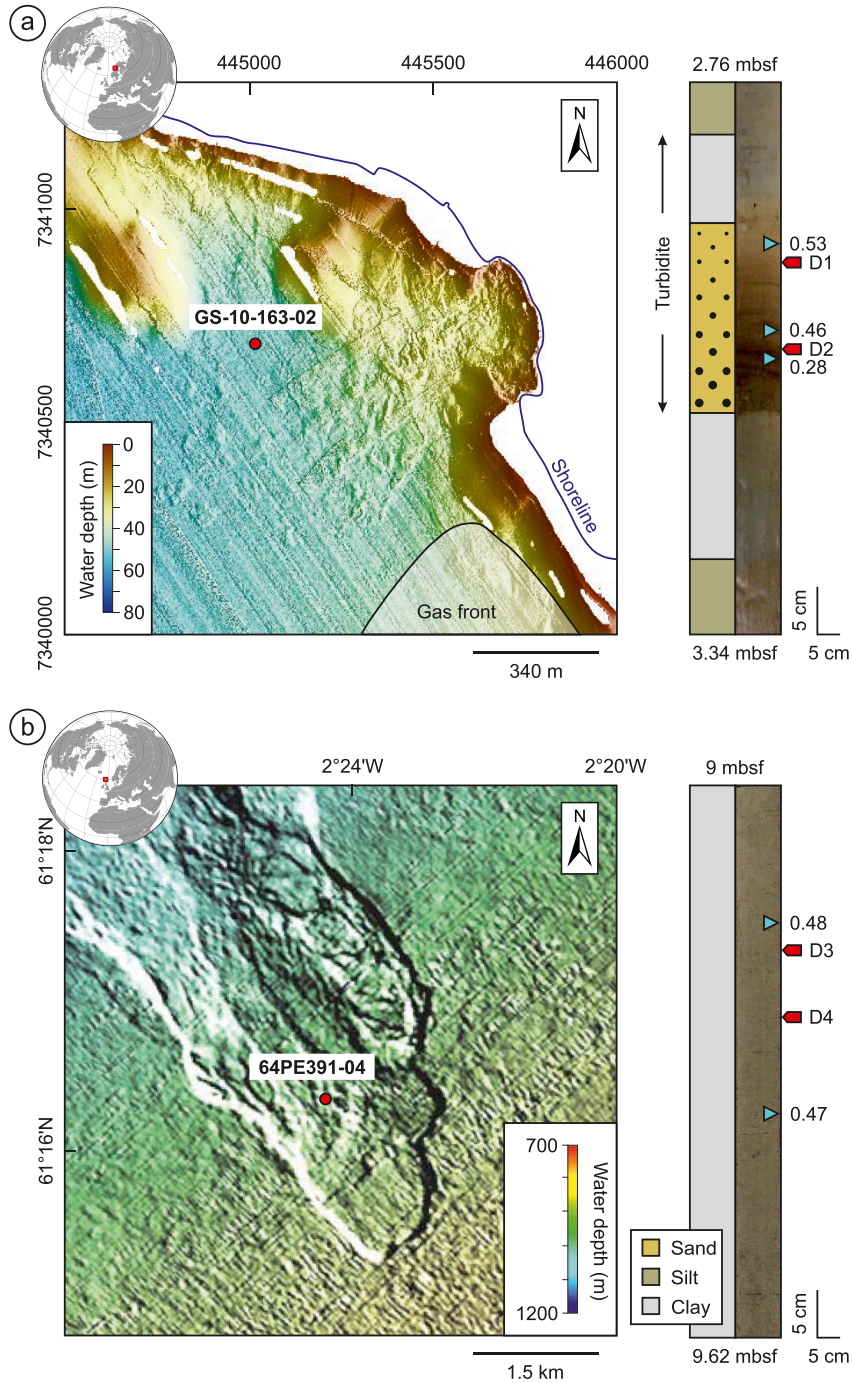

Figure 1. Core locations, Calypso piston core GS-10-163-02 (a; Projection in UTM Zone 33°N coordinate system) and piston core 64PE391-04 (b), are shown as red dots. Photographs and stratigraphy of both cores are shown with sample locations (D1–D4) outlined in red and water content measurements and locations indicated as blue triangles (Gatter et al., 2020; Vardy et al., 2012). Bathymetric data from (a) Vanneste et al. (2011) and (b) Wilson et al. (2005).

from a homogeneous sediment unit that consists predominantly of silty clay and was linked to steady glacio-marine sediment deposition (Gatter et al., 2020). All four cylindrical samples were collected using a miniature cutting tool (Clayton et al., 1995) that is made of stainless steel attached at the front of a carbon fiber tube to contain the sample as it is driven. Carbon fiber tubes (internal diameter 3 mm, height 7 mm, wall thickness 1 mm)

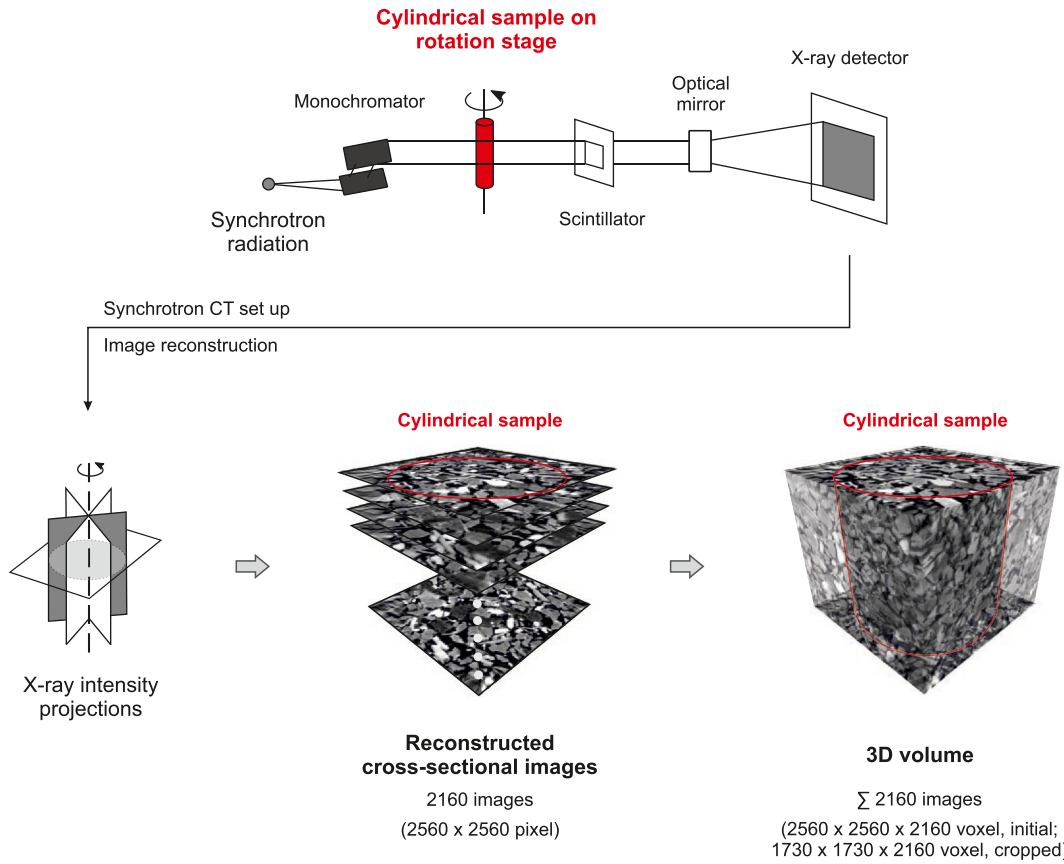

Figure 2. Synchrotron X-ray CT set up and image reconstruction (after Chung et al., 2019). The original cylindrical field of view, that is, the center of the sample, is outlined in red.

were chosen because of the material's low density that allows X-rays to pass through without or with minimum attenuation (i.e., transparent in scans), which makes it suitable for CT imaging.

3.2. Synchrotron X-Ray Computed Tomography

3D μCT imaging was performed, using monochromatic X-rays from a synchrotron source, at the TOMCAT Beamline of the Swiss Light Source (SLS), Paul Scherrer Institute, Switzerland. For this study, a beam energy of 21 keV and a propagation distance of 81 mm were used to scan the selected samples. Per sample, 1,501 projections (over 180° sample rotation) were recorded with an exposure time of 200 ms. All settings were chosen after trial runs to obtain images at 0.325 μm voxel resolution. The total duration of an individual scan was 6 minutes. X-rays were converted to visible light using a Lutetium Aluminum Garnet (LuAG:Ce) scintillator, and magnified and recorded by sensitive CCD cameras (2,560 × 2,560 pixel, 10x objective). The projections were post-processed to generate light and dark corrected sinograms. These were in turn converted into 16-bit greyscale μCT volumes at a final 3D voxel resolution of 0.325 μm, using the phase reconstruction algorithm described by Paganin et al. (2002). The gray scale intensity range was based on the X-ray attenuation and refraction index of the expected mineralogical constituents of the scanned sediment (Moore et al., 2022). Initial "fast" scans were carried out in order to identify the ideal section of the sample to obtain high-resolution scans. The inner, middle part of the sample generally did not show any disturbances from the sampling process, and was, therefore, selected to be scanned by excluding the outer 1 mm annulus of the core from the field of view. Each reconstructed 3D volume consists of 2,160 individual 2D cross-sections, or slice images (2,560 × 2,560 pixel), which are stacked together. The procedure of data acquisition is illustrated in Figure 2 (e.g., Chung et al., 2019).

3.3. Data Analysis

The μCT data were processed and analyzed with Avizo 3D (version 2022.1) and Fiji ImageJ (Schindelin et al., 2012). The 2D cross-sectional images of all four samples were first cropped to 1,730 × 1,730 pixel in order to accommodate only the field of view, that is, the centre of the sample, in the reconstructed 3D volume (Figure 2). The size of the final 3D volumes, which were used for further analyses, was 1,730 × 1,730 × 2,160 voxel at a voxel resolution of 0.325 μm for all four samples. The final sample size (dimensions of the 3D volumes) was therefore 562.25 × 562.25 × 702 μm.

3.3.1. Image Segmentation

To identify, characterize and analyze different components of the samples, for example, particles and pores, an image "segmentation" based on gray values of the reconstructed 3D volume (or 2D images) must be applied to the full μCT data sets. This segmentation is simply a rule-based selection about whether a voxel (or pixel) belongs to a certain material or not. Here, we used a combination of two segmentation methods to segment the reconstructed 3D volumes into three phases: a *pore*, *particle* and *mixed* phase.

First, a machine-learning method (Trainable Weka Segmentation 2D, Arganda-Carreras et al., 2017), available as a plugin for Fiji, was used to segment the reconstructed 2D greyscale images into two phases (termed "classes" in Fiji and "labels" in Avizo 3D): a *pore* phase, consisting of pores and pore throats, and a preliminary *solid* phase consisting of sediment grains and particles, respectively. Trainable Weka Segmentation was chosen over an absolute thresholding method, because it has the advantage of utilizing spatial information rather than gray values alone and therefore, performs better on the recognition of complex shapes of individual particles and pores (Berg et al., 2018). The classifier training in Fiji was based on a combination of shape recognition of individual grains, particles and pores, as well as gray value thresholding (Figure 3; see Text S1 and Figure S1 in Supporting Information S1 for more details).

The results obtained from the Trainable Weka Segmentation were subsequently deployed as input data for a marker-based watershed algorithm segmentation (*Watershed* module in Avizo 3D), which was used to separate the solid phase into a *mixed* phase consisting of a mixture of water and fine-grained particles, and a *particle* phase comprising recognizable sediment grains and particles. The watershed algorithm is a region-based technique that uses image morphology for segmentation (e.g., Schlüter et al., 2014). The method requires the selection of "seeds" (or markers) for the different objects of the image, that is, in our case, particles and pore space. The pore phase resulting from the Trainable Weka Segmentation was used as seed for the pore space, while the particle markers were set with the *SegmentationEditor* by threshold segmentation (thresholds for samples: D1 >23,000, D2 >26,500, D3 >21,000, D4 >16,000). The resulting images consisted of the pore space (the *pore* phase + the new *mixed* phase) and the sediment particles (the new *particle* phase; see Text S2 in Supporting Information S1 for more details). Note that for the watershed segmentation, the samples had to be resampled to 1 μm spatial resolution, because of computational limitations.

3.3.2. Porosity Calculations

Quantitative analyses were performed on the segmented pore and mixed phases of all four scanned samples. Porosity profiles were computed for each 3D volume using the area fraction of (a) the pore phase and (b) the pore + mixed phase in each reconstructed 2D image, ranging from 0 to 702 μm sample depth. The 3D volume fraction of the segmented pore + mixed phase was used to calculate the bulk porosity of each sample. X-z, y-z and x-y cross-sections through the 3D volume were used to calculate average porosities and porosity changes over sample depth/width in 2D (Figure 4). The total area fraction of the segmented pore + mixed phase in the 2D cross-sections was used to calculate the samples' average porosities in 2D. Porosity profiles throughout 2D cross-sections were obtained by means of pixel counts per row of the pore + mixed phase (ranging from 0 to 702 μm sample depth in x-z and y-z cross-sections, and ranging from 0 to 562.25 μm sample width in x-y cross-sections).

4. Results

An overview of all four analyzed sediment samples used in this study is shown in Figure 4. These four sediment samples were analyzed by means of high-resolution μCT imaging and segmented, based on the differences in gray

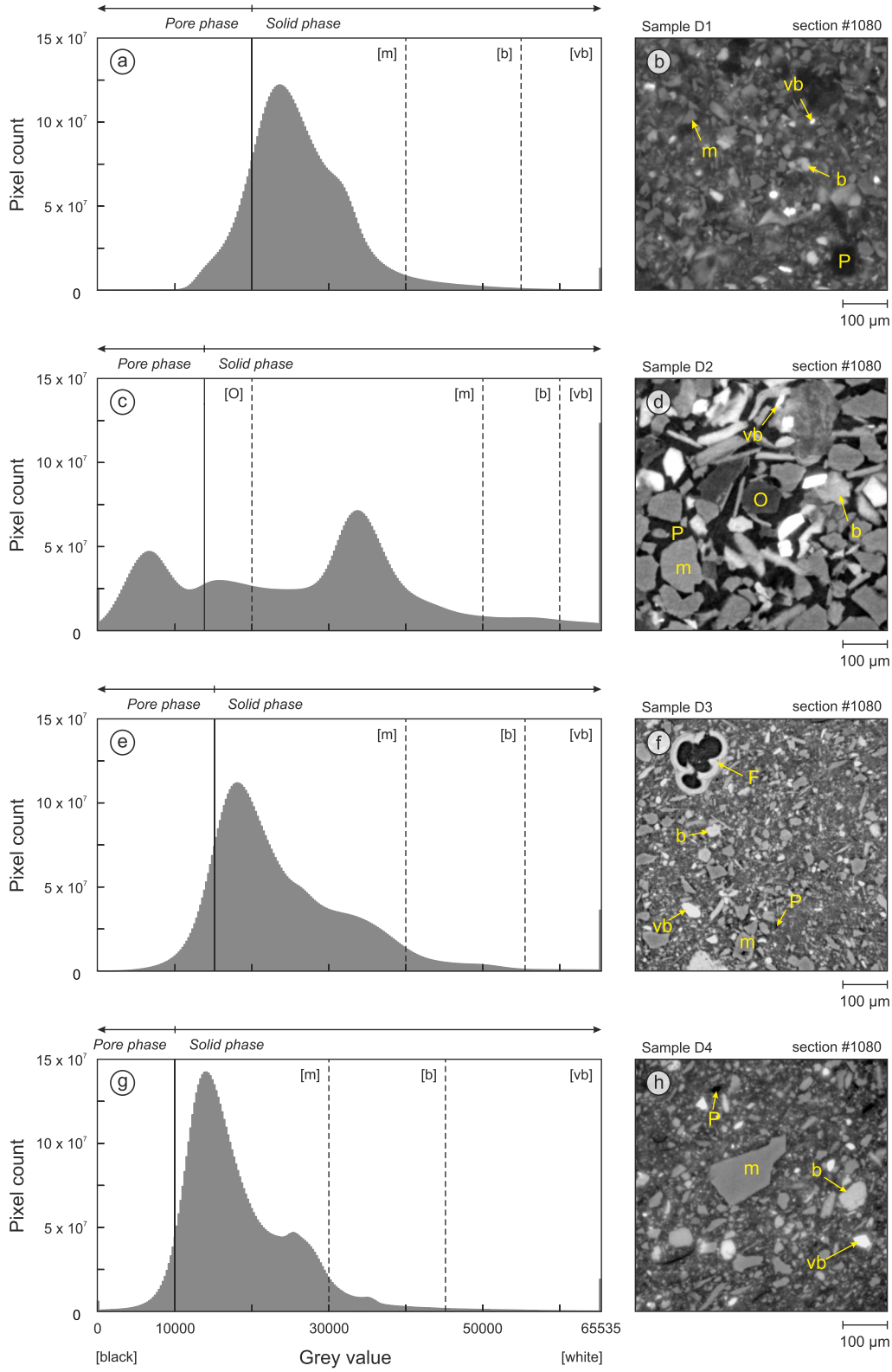

Figure 3.

values in the reconstructed 3D volumes, into three phases: the *particle* phase, which consists of recognizable sediment grains and particles, the *pore* phase, which consists of recognizable pores and pore throats, and the *mixed* phase, which represents a mixture of very fine-grained particles (or organic material) and small pores that cannot be further separated due to resolution limitations (Figure 5).

The *particle* phase of the analyzed samples consists predominantly of non-biogenic sediment and lesser amounts of biogenic components (sample D3 and D4). Although one of the known constraints of CT systems is the discrimination of mineral types (e.g., Guntoro et al., 2019), based on the difference in gray values, the non-biogenic sediment components could be classified into three main classes: (a) very-high density (very bright) grains, (b) high density (bright) calcareous grains, most likely calcite, and (c) medium density (medium bright) siliceous grains (Figure 3). The classification into high- and medium density grains is further affirmed by the presence of foraminifera and diatoms in the sediments (sample D3 and D4, Figure 4) that are calcareous and siliceous, respectively, which allows a rough mineralogical classification of the non-biogenic components based on similar gray values (Figure 3).

The *pore* phase in all four reconstructed 3D volumes is characterized by very low gray values (Figure 3). Based on the gray values, the pore space appears to be completely water-filled in sample D1, D3 and D4. In contrast, the pore space in sample D2 shows even lower gray values and appears to be largely devoid of water (peak in gray value around 7,500 in Figures 3 and 4).

The *mixed* phase of three samples, D1, D3 and D4, consists of a mixture of water and clay. In contrast to the finer-grained samples, the mixed phase of sample D2 consists predominantly of organic material (around 9.8% of the total sample volume). This organic material is characterized by noticeably lower gray values than the particle phase and higher gray values than the pore phase of the sample (Figure 3). It can be recognized by its form and distribution throughout the sample, typically filling the pore space between individual grains.

4.1. Sandy Sediment Samples

Two sediment samples (D1 and D2) were taken from a sandy layer and served as representative endmembers of a coarse-grained material. A classification based on gray values reveals that more than 90% of the sediment grains in sample D1 and more than 65% of sediment grains in sample D2 have the same density, most likely quartz and phyllosilicates, with smaller amounts of high-density (most likely calcite) and very high-density grains in both samples (Figures 3 and 4a–4h). In addition to individual grains and particles, a small number of mineral-aggregates, that is, combined mineral mixtures, could be identified in sample D2 (Figures 4f–4h). Organic material (about 9.8%) could be identified by its characteristic lower density (Figure 3) and structure in sample D2 (Figures 4e–4h). The pore space in both samples is characterized by very low gray values (<20,000 in D1 and <14,000 in D2; Figure 3). Slightly higher gray values in sample D1 are related to the presence of water in the pores space, while the pore space of sample D2 appears to be largely devoid of water (Figures 4a–4h).

4.1.1. Visual Description

Sample D1, which was taken from the upper section of the sandy layer (at 2.95 mbsf), consists of predominantly elongated, very-fine sand-sized and sub-angular, silt-to-very-fine sand-sized grains embedded in a matrix of very-fine-silt to clay-sized particles (Figures 4b–4d). Elongated grains appear sub-horizontally bedded with a preferential orientation parallel to the x-y plane in the 3D volume (Figures 4b and 4c). The pore network consists of discernible large (up to 100 μm), flat, ellipsoid pores (Figures 4a–4c) that are connected to smaller (<10 μm) pores by pore throats (Figures 4a–4d). Pores are generally characterized by irregular surfaces and show a preferential orientation in accordance with the elongated grains (Figures 4b and 4c).

In contrast to D1, sample D2, which was taken from the lower section of the sandy layer (at 3.04 mbsf), is coarser-grained and consists predominantly of fine-to-very-fine sand-sized grains, with a noticeable amount of organic

Figure 3. Gray scale histograms and 2D cross-sectional images of sample D1 (a), (b), D2 (c), (d), D3 (e), (f) and D4 (g), (h). Histograms are calculated over the entire 3D volumes and show the gray value distribution for each sample over 255 bins. Solid lines outline the gray value thresholds used as input for pore and solid phase segmentation. Dashed lines indicate thresholds used to divide the particle phase into sub-classes (organic material, and medium density (medium bright), high density (bright) and very high-density (very bright) grains). Greyscale image #1080 (x-y cross-section at 351 μm sample depth) is shown for samples D1–D4 (b, d, f, h). *P = pores*, *m = medium bright*, *b = bright*, *vb = very bright*, *O = organic material, F = foraminifera*.

10.1029/2024GC011840

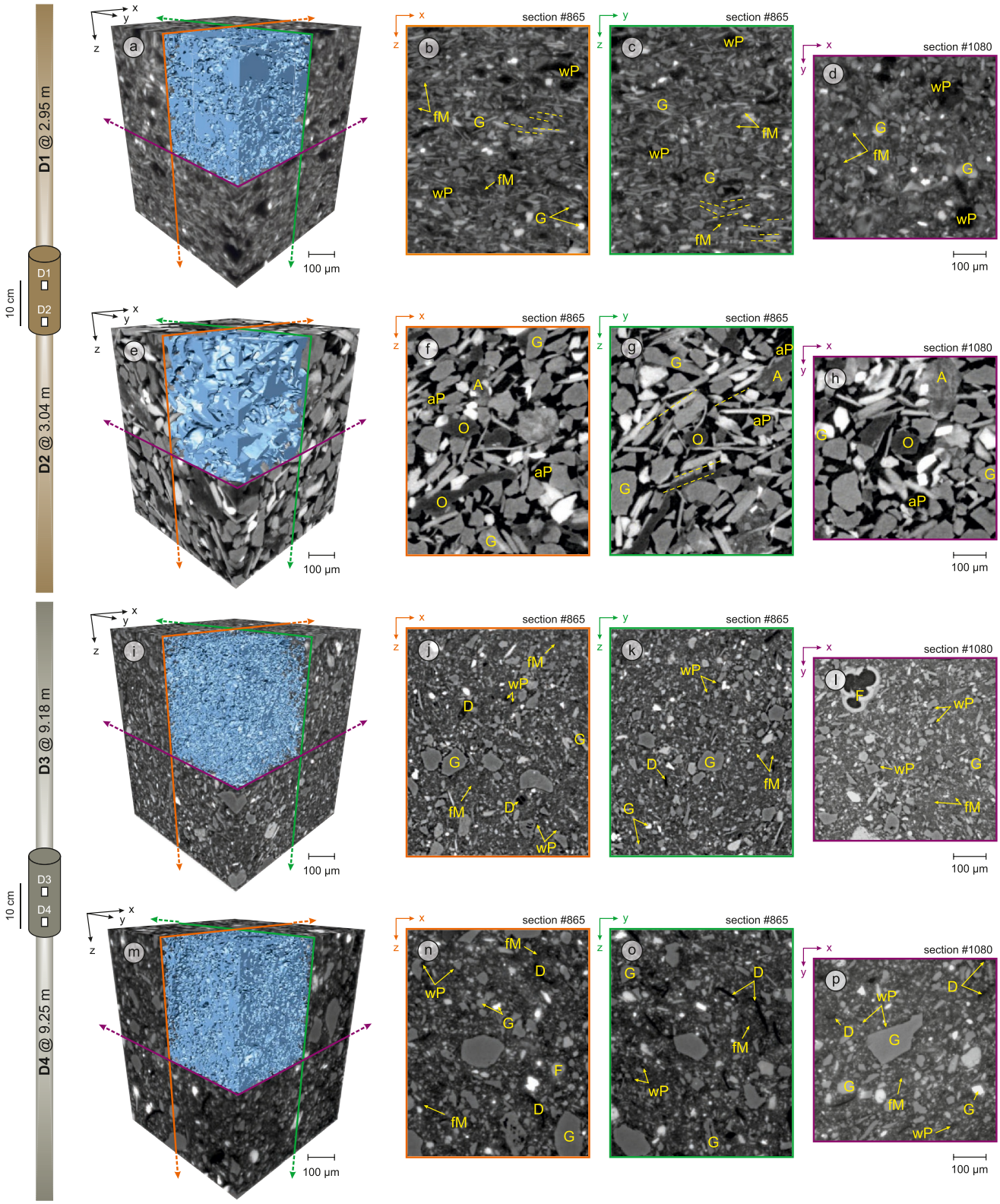

Figure 4.

material (approximately 9.8%) and a small amount of aggregates (Figures 4e–4h). Sediment grains are mainly sub-angular or elongated. The organic material, as well as the aggregates, are heterogeneous with irregular surfaces and complex internal structures (Figures 4f–4h). Both the grains and the organic material, appear to have a preferential orientation sub-parallel to the x-y plane in the 3D volume (Figures 4f and 4g). The pore structure is characterized by large, angular pores with few or no obvious pore throats.

4.1.2. Porosity Calculations

The reconstructed pore space shown in Figure 4 was used to compute the average porosity over the entire 3D volumes (bulk porosity), as well as for three x-z, y-z and x-y cross-sections through each 3D volume (Table 1). The bulk porosities of the sandy samples, D1 and D2, are 0.38 and 0.40, respectively. Average porosities obtained from 2D information, that is, x-z, y-z and x-y cross-sections, of sample D1 are the same or slightly lower than the bulk porosity (Table 1), and range from 0.37 to 0.42 for sample D2 (Table 1).

Figure 6 shows porosity profiles obtained for both sandy samples and compares changes in porosity estimates from 3D and 2D data. In particular, the variability in porosity profiles related to different orientations and locations of 2D cross-sections is highlighted (orange, green and purple color codes in Figure 6). Although average porosity estimates for 2D x-z, y-z and x-y cross-sections are within the same range in samples D1 and D2, respectively (Table 1, Figure 6), depending on the location of the 2D cross-sections, the related porosity profiles show variability. X-z and y-z porosity profiles of sample D1 appear to undulate around the average porosity (Figures 6b and 6c), while x-y profiles show a subtle change in pattern. In the x-y profiles, porosities first decrease slightly until about 300 µm sample width and remain overall constant between 300 and 562.25 µm (Figure 6d).

In sample D2, a shift in porosity change frequency (i.e., distance between maxima and minima) can be observed in x-z profiles at around 500 µm sample depth (Figure 6f). Similar shift can be observed in y-z profiles at around 600 µm sample depth (Figure 6g). The x-z and y-z porosity profiles have an overall constant pattern and mainly undulate around the average porosity. X-y porosity profiles show slightly increasing values until 400 µm width. At 400 µm, a shift towards lower porosity can be observed, after which porosities increase in the x-y profile (dark purple; Figure 6h). The depth-dependent changes have a higher frequency (i.e., shorter distance between maxima and minima) in sample D1 than sample D2.

4.2. Silty-Clay Sediment Samples

Samples D3 and D4 were taken from a silty clay unit and served as representative endmembers of a fine-grained material. A classification based on differences in gray values allows a distinction between three density fractions in the particle phase: medium-, high- and very high-density sediment particles and grains (medium bright, bright and very bright; Figure 3). The high- and very high-density fractions are most likely related to calcareous and iron-rich minerals, while the medium density fraction consists most likely of quartz and phyllosilicates (Figures 4i–4p). Biogenic components (foraminifera and diatoms) could be identified based on their morphology (Figures 4i–4p). The pore space in both samples is characterized by very low gray values (<15,000 in D3 and <10,000 in D4; Figure 3) and appears to be water-filled (Figures 4i–4p).

4.2.1. Visual Description

Sample D3 was taken from a silty clay unit and consists of sediment grains of variable size, ranging from larger, silt to very-fine-sand-sized grains to smaller, fine-silt-sized grains that are embedded in a fine-grained matrix (Figures 4j–4l). Sediment grains are either platy or sub-angular shaped. In addition to these grains, foraminifera and diatom frustules can be observed (Figures 4j–4l). Foraminifera are relatively large, up to about 150 µm in diameter and their shells appear to be largely preserved within the samples. Diatom frustules are mostly elongated and curved with lengths ranging from <20 µm to more than 120 µm. In contrast to foraminifera, the majority of diatom frustules appear to be dissolved. Although the original shape of the frustules can be seen in the 3D

Figure 4. 3D volume (a, e, i, m) and 2D x-z (b, f, j, n), y-z (c, g, k, o) and x-y (d, h, l, p) cross-sections of the sand (D1 and D2) and clay (D3 and D4) samples. Position of cross-sections within the 3D volumes are outlined in orange (x-z), green (y-z) and purple (x-y). X-z (orange outlined) and y-z (green outlined) cross-sections are computed at 281 µm sample width and x-z cross-sections (purple outlined) at 351 µm sample depth. Window in 3D volumes shows the reconstructed pore space in blue. *fM = fine-grained matrix, wP = water-filled pores, G = grain, aP = air-filled pores, A = aggregate, O = organic material, D = diatom, F = foraminifera*. Preferential particle and pore orientation of D1 and D2 outlined in yellow (b, c, g).

10.1029/2024GC011840

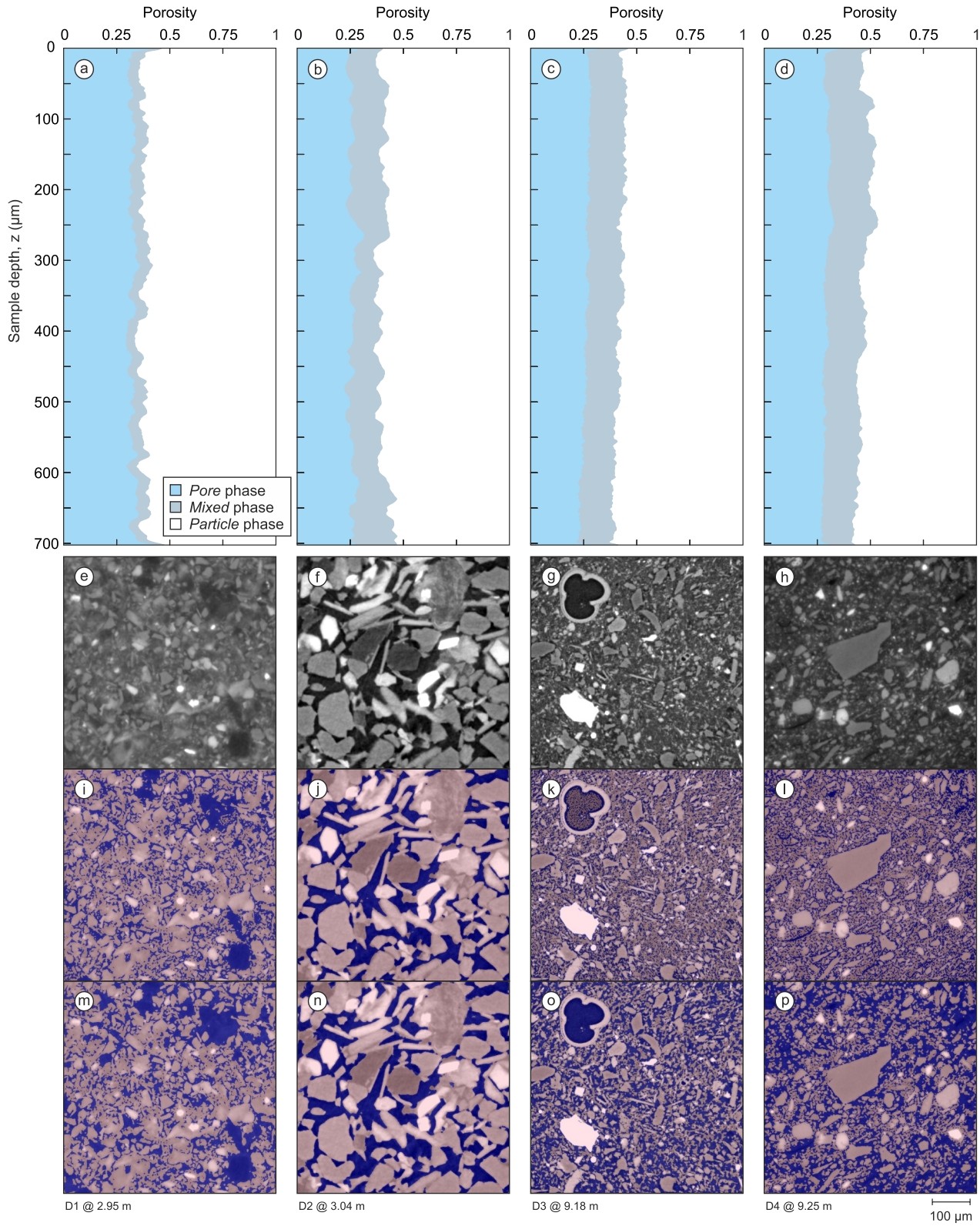

Figure 5.

volumes, no traces of the frustule walls can be seen (Figures 4j–4l). This observation suggests that large parts of the diatom frustules could have been dissolved after core recovery during storage. The pore network consists of small (<10 μm) pores that are connected via pore throats (Figure 4i). Larger pores (>50 μm) are related to pores of the biogenic material (Figures 4i–4l). The pore space appears to be water-filled.

Similar to D3, sample D4 consists of sub-rounded sediment grains that range in size from larger, very-fine-sand-sized to smaller, fine-silt-sized grains that are generally matrix-supported (Figures 4m–4p). The biogenic components consist predominantly of diatom frustules (<15 μm to >170 μm in length) with some (up to 85 μm in size) foraminifera (Figures 4n–4p). The pore structure is characterized by mainly small pores that appear to be water-filled and connected by pore throats. Larger pores (up to 90 μm) are related to the presence of biogenic material.

4.2.2. Porosity Calculations

The bulk porosity, obtained from the 3D reconstructed pore space in Figure 4, of sample D3 is 0.42 and 0.47 for sample D4 (Table 1). Average porosities obtained from 2D x-z, y-z, and x-y cross-sections through the 3D volumes of the silty clay range from 0.39 to 0.43 in sample D3, and show quite high variability in sample D4, with estimated porosities ranging from 0.39 to 0.51 (Table 1).

Variability in average porosity estimates and porosity profiles obtained from 2D cross-sections are compared to the bulk porosity and 3D profiles of sample D3 and D4 in Figure 7. Average porosity estimates obtained from 2D cross-sections show little difference in sample D3. The greatest variability is shown in porosity estimates obtained from x-z cross-sections through sample D4, which range from 0.25 to 0.30 (Table 1, Figure 7f). Independent of orientation and location of 2D cross-sections in the 3D volumes, high-frequency porosity changes can be observed in both samples, D3 and D4 (Figure 7).

The X-z and y-z profiles of sample D3 show almost constant to slightly decreasing porosity values with sample depth (Figures 7b and 7c). Porosity profiles obtained from x-y cross-sections through sample D3 are almost constant until around 400 μm width, where a step in the profiles and shift to overall high porosity values can be observed (Figure 7d). In sample D4, porosity appears to decrease slightly with sample depth (x-z profiles; Figure 7f). In contrast, y-z profiles appear almost constant over the entire sample depth (Figure 7g). In x-y profiles, porosity first decreases until around 300 μm sample width before starting to increase (Figure 7h).

5. Discussion

This study provides structural information on two marine lithological end-members: (a) a coarse-grained sandy sediment and (b) a fine-grained silty clay sediment obtained from high-resolution 3D μCT data. Analyzing the μCT data, it was possible to extract quantitative porosity values and qualitative pore space information in 3D. It was found that silty clay samples generally have slightly higher porosities in comparison to sandy samples (Table 1). In addition, 3D pore space reconstruction of the samples revealed significant differences in pore size, shape and distribution, not only between lithological endmembers, but also between samples taken from the same lithological units (Figure 4). These differences in micro-scale pore space can be attributed, in part, to inherent physical properties of the analyzed sediment types, for example, larger pores are found within the coarse-grained samples (Figure 4). Such micro-scale variations in sediment properties are usually not resolvable with conventional sediment core analytical techniques (e.g., L'Heureux et al., 2012; Steiner et al., 2012; Vanneste et al., 2011, 2013, 2014; Vardy et al., 2012), but may have a significant impact on macro-scale properties such as fluid flow dynamics.

5.1. From Macro- to Micro-Scale Sediment Characterization

Samples D1 and D2 were taken from a prominent fining-upwards sand layer identified in a sediment core in a fjord near the village of Finneidfjord, Norway (L'Heureux et al., 2012; Vanneste et al., 2011). L'Heureux

Figure 5. Comparison of porosity estimates for samples D1–D4. (a–d). Porosity is expressed as a fraction varying between 0 and 1 over the sample depth (z) with blue indicating porosity based on the pore phase, gray showing the mixed phase and white the particle phase. (e–p) show the x-y cross-section at 351 μm depth for samples D1–D4, the original greyscale images (e–h), the segmented images after Trainable Weka Segmentation (i–l) and the segmented images after watershed segmentation that were used for bulk porosity estimations (m–p). Note that the pore space (blue) in panels (e–h) is estimated using the pore phase alone, while in panels (m–p) the pore space (blue) is estimated using the pore + mixed phase.

Table 1
Porosity Estimates for Samples D1, D2, D3, and D4 Over the Entire 3D Volumes (Bulk Porosity) and 2D Cross-Sections Through the 3D Volumes

			Sample			
			Sand		Clay	
Cross-section			D1	D2	D3	D4
2D	x-z	@ 141 μm	0.38	0.42	0.42	0.48
		@ 281 μm	0.36	0.40	0.40	0.39
		@ 423 μm	0.38	0.40	0.43	0.46
	y-z	@ 141 μm	0.35	0.41	0.42	0.46
		@ 281 μm	0.36	0.40	0.39	0.43
		@ 423 μm	0.38	0.37	0.40	0.48
	x-y	@ 175 μm	0.37	0.40	0.44	0.51
		@ 351 μm	0.35	0.37	0.44	0.45
		@ 527 μm	0.36	0.38	0.40	0.44
3D			0.38	0.40	0.42	0.47

et al. (2012) related this sand layer to a turbidite or flow deposit. Our results confirm this relation and we interpret that the lower, coarser-grained sample (D2), is likely to be part of division A (massive to graded turbidite), while the upper sample (D1), which is generally finer-grained with a larger amount of silt-sized grains and characterized by elongated grains with a preferential orientation, can be related to division B-C (parallel laminae—ripples and convolute bedding) of the Bouma sequence (Bouma, 1962). In addition to differences in grain size and morphology between the lower (D2) and upper (D1) parts of the sand layer, clear changes in the pore space can also be observed (Figure 4). The lower sample D2 has a large, connected pore space with no clear difference between pores and pore throats. This pore space appears to be largely devoid of water (Figure 4), which could have been the result of water loss during sub-sampling. A water content of 0.28 just below sample D2 (Figure 1), however, suggests that the sediment was never fully saturated or that water loss had already occurred prior to sub-sampling. In contrast, the upper sample D1 is characterized by a water-filled pore space with individual large pores that are connected via pore throats. In comparison to the overall grain size, these individual pores are rather large. The prominent shape (flat, ellipsoid) and size of the pores raises the question if these are just trapped pores or if other processes caused their formation.

One potential explanation for these large pores could be fluid escape structures. Turbidites can have fluid escape structures (e.g., Al-Mufti et al., 2022; Hage et al., 2017; Lowe, 1975; Robinson et al., 2021) that are typically expected to be vertically (orientated in z direction) aligned. Owing to the given stratigraphic sequence, a sand capped by a clay layer that may prevent vertical fluid escape; however, it is feasible that fluid escape would not have taken place vertically, but rather in the bed-parallel direction. Another possible origin would be the dissolution of organic material after which only the pore space remains. Considering the observations of organic material in sample D2 (Figure 4), however, we would expect the large pores in sample D1 to resemble the shapes of the organic material in sample D2 more closely. In addition, if the organic material is preserved in sample D2, it is unlikely to have been completely dissolved in sample D1. In contrast, we would expect to be able to observe at least some remainders of organic material in sample D1 as well. Vesicular spots indicative of gas bubbles have previously been reported for sediment cores in this fjord, but were linked to organic run-off from the modern shoreline (L'Heureux et al., 2012). Although the occurrence of free gas was also reported, this free gas was found about 800 m south of the study area and forms a well-defined gas front much closer to the input from the Nidelva River (Longva et al., 2003; Morgan et al., 2012). Therefore, the most likely explanation for the observed pores (Figure 4) is the lateral movement of pore fluids along the bedding plane (Vardy et al., 2012).

Samples D3 and D4 were taken from a homogeneous sediment unit consisting of silty clay that was linked to steady glaciomarine sediment deposition in the Faroe-Shetland Channel, offshore Northern Scotland (Gatter et al., 2020). In contrast to the coarse-grained samples (D1 and D2), the fine-grained samples (D3 and D4) show less variability in their composition, grain size and morphology, as well as in their pore spaces (Figure 4). Gatter et al. (2020) reported relatively high fractional porosity (>0.5) and water content (~48%) for the sampled unit, which is similar to porosity values (~0.39–0.51) obtained from μCT imaging (Table 1). The pore space in both samples, D3 and D4, appears to be influenced by the presence of microfossils in the sediments (Figures 3 and 4). Peak (porosity) distribution in porosity profiles (Figure 7) can therefore be mainly related to the presence or absence of biogenic material in the sample.

The biogenic material in samples D3 and D4 mainly consists of foraminifera and diatom frustules (Figure 4). Although the shape of diatom frustules is visible in the 3D volumes, these structures are negative imprints, that is, only the pore space related to the diatom frustules remains while the shells appear to have been dissolved. The dissolution of diatom frustules likely occurred after core recovery during sediment core storage. If dissolution had taken place within the sediment sequence, the overburden pressure of the overlying sediments would have likely caused compaction (e.g., Varkouhi et al., 2020; Volpi et al., 2003) and the frustule shapes would not have been preserved.

10.1029/2024GC011840

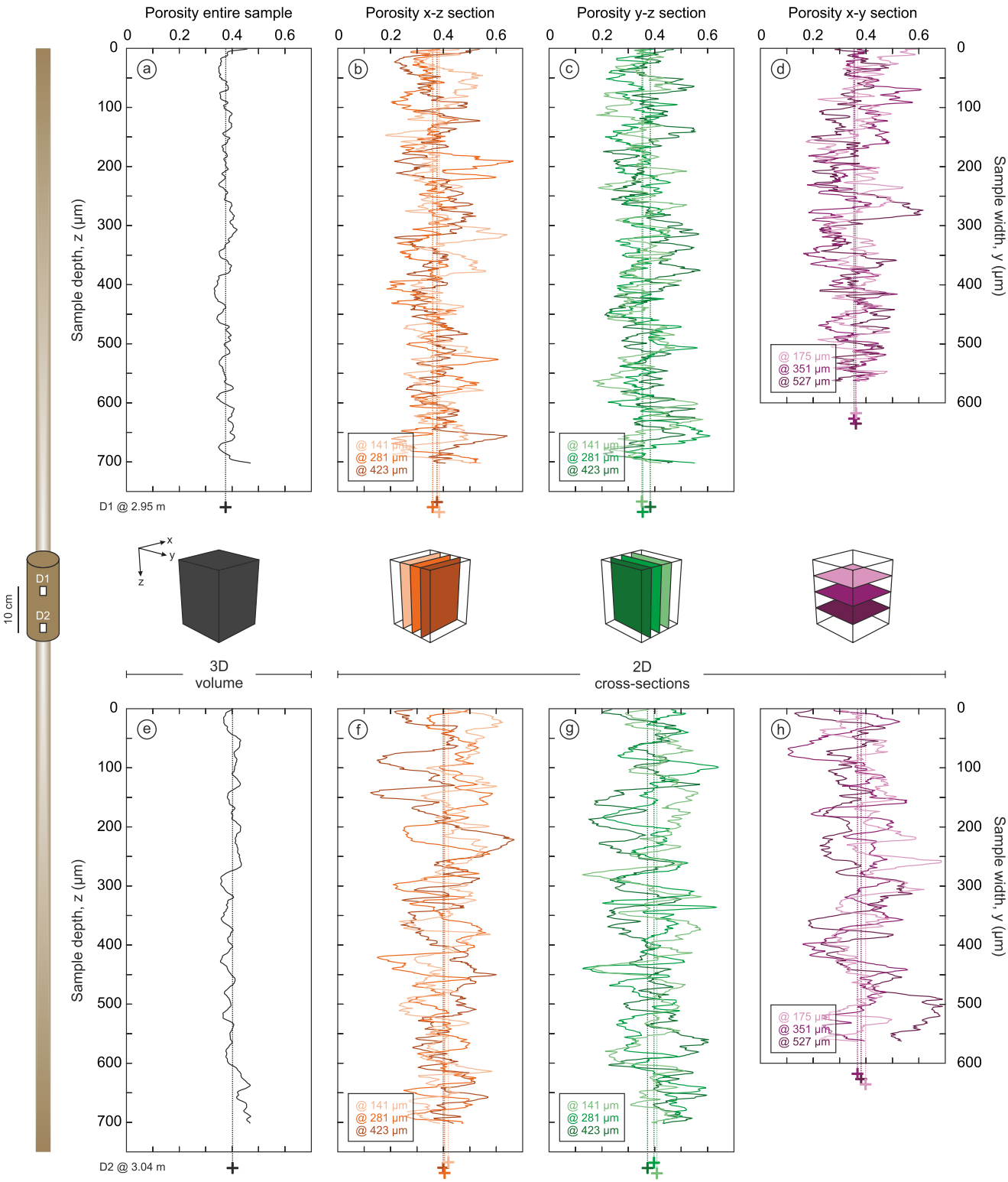

Figure 6. Porosity profiles for sand samples D1 (a)–(d) and D2 (e)–(h). Porosity variation with sample depth over the 3D volume in black (a), (e), over x-z cross-sections in orange (b), (f) and y-z cross-sections in green (c), (g). Porosity variations over x-y cross-sections in purple (d), (h) are shown. Mean porosities are outlined as dashed-lines with crosses below the diagrams. Positions of cross-sections at 141 µm, 281 µm, 423 µm and at 175 µm, 351 µm, 527 µm through the 3D volumes are outlined in miniature images.

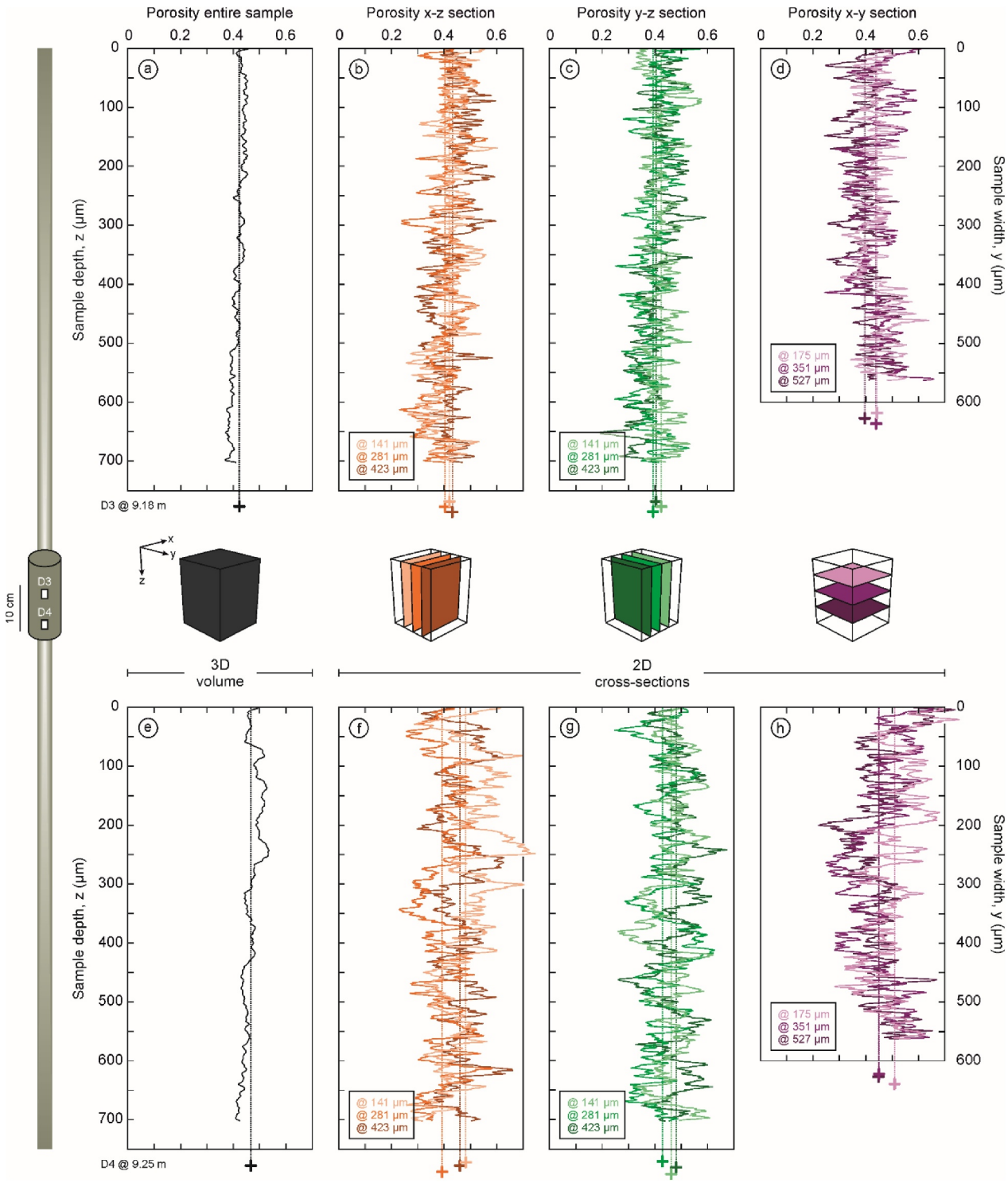

Figure 7. Porosity profiles for silty clay samples D3 (a)–(d) and D4 (e)–(h). Porosity variation with sample depth over the 3D volume in black (a), (e), over x-z cross-sections in orange (b), (f) and y-z cross-sections in green (c), (g), and porosity variation over x-y cross-sections in purple (d), (h) are shown. Mean porosities are outlined as dashed-lines with crosses below the diagrams. Positions of cross-sections at 141 µm, 281 µm, 423 µm and at 175 µm, 351 µm, 527 µm through the 3D volumes are outlined in miniature images.

Our data, from both a coarse-grained and fine-grained sediments demonstrate the value of high-resolution 3D image data. Variability in grain size and morphology, as well as pore space is clearly visible between samples that were taken from the same lithological units, only 9 cm apart (Figure 4). In general, silty clay samples have higher porosities in comparison to sandy samples (Table 1). The lowest porosity was obtained for sample D1 (Table 1), even though water measurements close to the sample location (Figure 1) indicate a higher porosity. This underestimation is likely linked to limitations in the image resolution, which could not be completely overcome by the introduction of a mixed phase in the overall analysis. Nevertheless, for sample D3 and D4, the mixed phase allowed for a better estimation of the porosity (Figure 5). For these fine-grained samples, it is crucial to take the water-clay mixture, that is, the segmented mixed phase, into account when estimating porosities.

The lower (initial) porosity value of the sandy sample D2, in turn, was mainly related to the presence of organic material in the sediment (Figure 3). During the Trainable Weka segmentation, the organic material was added to the solid phase. Organic materials, however, are characterized by high internal porosities (e.g., Katz & Arango, 2018; Sheng et al., 2020). This high internal porosity can also be observed in the gray-scale images (Figures 3 and 4f–4h). If the organic material is in turn considered as part of the pore space, the total porosity of sample D2 increases significantly (Figure 5, Table 1). Such small-scale changes cannot be resolved with other methods , such as geotechnical tests , which require larger (several centimeters) samples and would homogenize the results. In addition, the amount of sample material from sediment cores is very limited and often not suitable for further geotechnical analyses (e.g., Gatter et al., 2021; Jutzeler et al., 2014; Vanneste et al., 2014). Since µCT requires smaller samples, even small amounts of material can be used to obtain valuable information. Therefore, µCT can provide information of critical importance that is often missing from standard visual core descriptions or geotechnical investigations.

5.2. The Limitations of µCT When Investigating Marine Sediment Structures

Although the potential of X-ray CT is becoming more acknowledged in geosciences (e.g., Abbasi et al., 2022; Cnudde & Boone, 2013; Ketcham & Carlson, 2001; Mees et al., 2003; Wang & Miller, 2020; Zhang et al., 2019), the demands on the technique are also approaching its physical limitations. Several limiting factors have been identified and discussed in the literature (e.g., Cnudde & Boone, 2013; Sasov et al., 2008; Withers et al., 2021). A comprehensive overview would be outside the scope of this study; however, in the following we will discuss some limitations identified and directly related to the use of high-resolution µCT in particular to study marine sedimentary structures.

The application of µCT in geosciences requires a spatial resolution that is sufficient to reveal details of interest. To obtain high-quality results, high mechanical precision and stability of the object manipulator are required (e.g., Sasov et al., 2008). The best resolution and signal-to-noise ratio can usually be achieved by using synchrotron radiation (Baruchel et al., 2006; Maire & Withers, 2014). The high brilliance of the synchrotron radiation enables fast scanning at high spatial resolutions (e.g., 6 minutes for one sample with a voxel resolution of 0.325 µm in this study; Maire & Withers, 2014). The number of synchrotron facilities, however, is limited and operational costs are very high. Laboratory-based systems, on the other hand, are more cost effective but also have a lower X-ray flux, which limits the time resolution obtainable by these facilities (e.g., Bidola et al., 2017; Bultreys et al., 2016; Cnudde & Boone, 2013; Zwanenburg et al., 2021).

To properly detect and characterize features of interest (shape, volume, etc.), the selected voxel size of the reconstructed CT volume must be significantly smaller than the size of the expected feature (Saxena et al., 2017; Withers et al., 2021). Each voxel has a gray value, which is directly related to the effective linear X-ray attenuation in the corresponding voxel of the sample (e.g., Withers et al., 2021). If the voxel contains more than one material, such as the edge of a particle and pore, the effective linear X-ray attenuation is comprised of a volume-weight combination of the X-ray attenuation of the constituent materials (e.g., Tretiak & Smith, 2019). In addition, voxel values are also affected by materials outside the voxel bounds due to blurring. This becomes a problem when analyzing very fine-grained sediments with little to no separation and limited contrast. Our analysis of fine-grained sediment samples (D3 and D4, Figures 4 and 5) has shown that even with a voxel resolution of 0.325 µm it was difficult to discern clay particles. In addition, the segmentation of water-filled pores and fine-grained particles proved to be challenging due to overlapping gray value histograms (Figure 3). Likely, clay particles are partially dispersed in water, which causes the gray value to overlap. To overcome this challenge, further calibration through geochemical analysis and/or SEM is needed.

Similar to previous studies (e.g., Callow et al., 2020; Elkhoury et al., 2019; Saxena et al., 2017, 2019), we found that μCT systemically underestimated porosity in all four samples, and in particular in samples D3 and D4 (Figure 5) if only the pore phase (without the mixed phase) was considered. These sediments consist in large parts of a fine-grained matrix (Figures 4i–4p), which is a combination of fine-grained sediments and pore water. During the Trainable Weka image segmentation, the entirety of the sediment matrix was attributed to the solid phase, thereby overestimating the volume of fine-grained material and underestimating total porosity in the samples (Figure 5). To overcome this limitation, we introduced a mixed phase that accounts for the "slurry" material of our samples. For even better estimates, laboratory measured constraints, for example, geochemical investigation of sediment's mineralogy or SEM (Scanning Electron Microscopy) measurements of fine-grained sediment fraction for further calibration of gray scale thresholding, need to be implemented during image segmentation.

Although CT is a non-destructive method, image resolution is related to sample size or the recorded field of view on a detector (e.g., Withers et al., 2021); therefore, high-resolution μCT requires sub-sampling of sediment cores to sub-centimeter diameters (e.g., Cnudde et al., 2006). Great care is needed for this sub-sampling to not disturb the sample (e.g., Uramoto et al., 2014). In this study, no substantial deformation due to sub-sampling, such as cracks or preferential orientation of grains and pores along the sampling tube, was observed in the samples. In addition, it is important to consider where sub-samples should be taken. Therefore, the selection of adequate sub-samples requires sound pre-analysis of the sediment cores, which typically includes standard core-logging and physical property information that is ideally combined with whole-core CT scanning. We suggest that μCT scanning is therefore not a stand-alone method, and should rather be integrated in sediment core analytical workflows to obtain additional information.

6. Conclusion

This study explored the potential of high-resolution X-ray synchrotron micro-tomography (μCT) to investigate the textural and structural properties of natural marine sediments. To cover some of the diversity found in marine sediments, four samples were taken from two sediment cores that sampled marine sediments from a near-shore depositional regime and a submarine channel, respectively. Qualitative and quantitative structural information of two typical marine endmember lithologies, a coarse-grained sandy and a fine-grained silty-clay sediment, was compiled and analyzed in terms of the sediments' structural and compositional characteristics.

Clear structural differences are found between coarse- and fine-grained sediments, as well as between samples taken from the same lithological units. These differences can be attributed partly to different sediment types, that is, sandy versus silty-clay sediments, but also reveal a dependency on the sedimentation regime. We find that the pore space distribution is highly spatially variable and affects the sediment structure on a sub-millimeter scale. Such high variability may be masked by standard bulk porosity measurements, which require larger sediment samples and only provide information averaged over the entire sample. In addition, one porosity value can represent a wide range in heterogeneous pore spaces. Relying on 2D information alone may therefore falsify structural interpretations. The identification of small-(grain-)scale changes in 3D pore space and related sediment properties such as permeability, however, appears to be crucial to understand important geological processes, such as fluid flow through or the storage capacity of sediments.

Our results clearly demonstrate the huge potential of μCT to investigate the structure of natural marine sediments, in 3D, by obtaining information that is not resolved or lost in data acquired through other analytical methods. Despite the increased usage of (μ)CT in geosciences and its clear potential for structural investigations, the method still finds limited application, in particular for the investigation of marine sediments. This neglect can be related to some of the inherent limitations of the technique. From our data, we find uncertainties in computed sediment porosities induced by voxel resolution and contrast, which caused an underestimation of the computed porosities. This uncertainty is larger for fine-grained sediments than for coarse-grained sediments. In order to overcome such challenges, μCT imaging should be combined with other analytical methods and integrated into core analysis workflows. Combining standard core-logging and geotechnical analyses with 3D μCT will enable cross-validation of results and compensate for uncertainties and gaps in individual data sets.

Data Availability Statement

All raw μCT data used in this study (sample D1 = B043_20160307_SLS_1127_A3; sample D2 = B052_20160307_SLS_1127_A5, sample D3 = B019_20160303_SLS_1127_B04, sample D4 = B026_20160307_SLS_1127_A4), as well as the results obtained from the Trainable Weka segmentation, are available in the PANGAEA Data Repository (Gatter et al., 2025).

Acknowledgments
The authors thank the Paul Scherrer Institute, Villingen, Switzerland for providing synchrotron radiation beamtime at the TOMCAT-X02DA Beamline of the Swiss Light Source (SLS), Dr. Anne Bonnin and technical staff who assisted with the beam experiments that have contributed to this manuscript. Thanks also to the μ-VIS facility at the University of Southampton for image analysis capability and particularly to Prof. Ian Sinclair for his guidance with the proposal to TOMCAT and Dr Mark Mavrogordato for developing the sample holding rig for synchrotron imaging. We are grateful to Dr Maarten Vanneste of the Norwegian Geotechnical Institute, Dr Jo Brendryen of the University of Bergen (Norway) and Dr Suzanne MacLachlan (BOSCORF, U.K) for collaboration and providing access to the sediment cores. Constructive reviews by R. Ketcham and one anonymous reviewer significantly improved this manuscript. We also thank the British Ocean Sediment Core Research Facility for their technical support in this project. B. N. Madhusudhan was supported by the NERC Landslide-Tsunami risk to the UK (NE/K00008X/1) and Southampton Marine and Maritime Institute stimulus finding. G. Bartzke was supported by the BMBF DAM MultiMAREX project (03F0952E). Open Access funding enabled and organized by Projekt DEAL.

References

Abbasi, G. R., Arif, M., Isah, A., Ali, M., Mahmoud, M., Hoteit, H., et al. (2022). Gas hydrate characterization in sediments via x-ray micro-computed tomography. *Earth-Science Reviews*, *234*, 104233. https://doi.org/10.1016/j.earscirev.2022.104233

Al-Mufti, O. N., Arnott, R. W. C., Hinton, M. J., Alpay, S., & Russell, H. A. J. (2022). Using computed tomography (CT) to reconstruct depositional processes and products in the subaqueous glaciogenic Champlain Sea basin, Ottawa, Canada. *Geomorphology*, *403*, 108165. https://doi.org/10.1016/j.geomorph.2022.108165

Arganda-Carreras, I., Kaynig, V., Rueden, C., Eliceiri, K. W., Schindelin, J., Cordona, A., & Seung, S. H. (2017). Trainable Weka segmentation: A machine learning tool for microscopy pixel classification. *Bioinformatics*, *33*(15), 2424–2426. https://doi.org/10.1093/bioinformatics/btx180

Badhani, S., Cattaneo, A., Collico, S., Urgeles, R., Dennielou, B., Leroux, E., et al. (2020). *Integrated geophysical, sedimentological and geotechnical investigation of submarine landslides in the Gulf of Lions (Western Mediterranean)*. (Vol. 500, pp. 359–376). Geological Society, London, Special Publications. https://doi.org/10.1144/SP500-2019-175

Bartetzko, A., & Kopf, A. (2007). The relationship of undrained shear strength and porosity with depth in shallow (<50 m) marine sediments. *Sedimentary Geology*, *196*(1–4), 235–249. https://doi.org/10.1016/j.sedgeo.2006.04.005

Baruchel, J., Buffiere, J. Y., Cloetens, P., Di Michiel, M., Ferrie, E., Ludwig, W., et al. (2006). Advances in synchrotron radiation micro-tomography. *Scripta Materialia*, *55*(1), 41–46. https://doi.org/10.1016/j.scriptamat.2006.02.012

Bendle, J. M., Palmer, A. P., & Carr, S. J. (2015). A comparison of micro-CT and thin section analysis of Lateglacial glaciolacustrine varves from Glen Roy, Scotland. *Quaternary Science Reviews*, *114*, 61–77. https://doi.org/10.1016/j.quascirev.2015.02.008

Bennet, R. H., Fischer, K. M., Li, H., Baerwald, R., Hulbert, M. H., Yamamoto, T., & Badiey, M. (1990). In situ porosity and permeability of selected carbonate sediment: Great Bahama bank Part 2: Microfabric. *Marine Geotechnology*, *9*(1), 29–47. https://doi.org/10.1080/10641199009388228

Berg, S., Saxena, N., Shaik, M., & Pradhan, C. (2018). Generation of ground truth images to validate micro-CT image-processing pipelines. *The Leading Edge*, *37*(6), 412–420. https://doi.org/10.1190/tle37060412.1

Bidola, P., Morgan, K., Willner, M., Fehringer, A., Allner, S., Prade, F., et al. (2017). Application of sensitive, high-resolution imaging at a commercial lab-based X-ray micro-CT system using propagation-based phase retrieval. *Journal of Microscopy*, *266*(2), 211–220. https://doi.org/10.1111/jmi.12530

Bouma, A. H. (1962). Sedimentology of some flysch deposits. In *A graphic approach to facies interpretation* (p. 168). Elsevier.

Brown, C. J., Sameoto, J. A., & Smith, S. J. (2012). Multiple methods, maps, and management applications: Purpose mode seafloor maps in support of ocean management. *Journal of Sea Research*, *72*, 1–13. https://doi.org/10.1016/j.seares.2012.04.009

Bultreys, T., Boone, M. A., Boone, M. N., De Schryver, T., Masschaele, B., Van Hoorebeke, L., & Cnudde, V. (2016). Fast laboratory-based micro-computed tomography for pore-scale research: Illustrative experiments and perspectives on the future. *Advances in Water Resources*, *95*, 341–351. https://doi.org/10.1016/j.advwatres.2015.05.012

Callow, B., Flacon-Suarez, I., Marin-Moreno, H., Bull, J. M., & Ahmed, S. (2020). Optimal X-ray micro-CT image based methods for porosity and permeability quantification in heterogeneous sandstones. *Geophysical Journal International*, *223*(2), 1210–1229. https://doi.org/10.1093/gji/ggaa321

Chen, B., Sun, D., & Yun-shi, H. (2020). Experimental study on strength characteristics and microscopic mechanism of marine soft clays. *Marine Georesources & Geotechnology*, *38*(5), 570–582. https://doi.org/10.1080/1064119X.2019.1604917

Chung, S. Y., Kim, J. S., Stephan, D., & Han, T. S. (2019). Overview of the use of micro-computed tomography (micro-CT) to investigate the relation between the material characteristics and properties of cement-based materials. *Construction and Building Materials*, *229*, 116843. https://doi.org/10.1016/j.conbuildmat.2019.116843

Clayton, C. R. I., Simons, N. E., & Matthews, M. C. (1995). *Site investigation* (p. 424). Wiley-Blackwell.

Cnudde, V., & Boone, M. N. (2013). High-resolution X-ray computed tomography in geosciences: A review of the current technology and applications. *Earth-Science Reviews*, *123*, 1–17. https://doi.org/10.1016/j.earscirev.2013.04.003

Cnudde, V., Masschaele, B., Dierick, M., Vlassenbroeck, J., Van Hoorebeke, L., & Jacobs, P. (2006). Recent progress in X-ray CT as geosciences tool. *Applied Geochemistry*, *21*(5), 826–832. https://doi.org/10.1016/j.apgeochem.2006.02.010

Cornard, P. H., Degenhart, G., Tropper, P., Moernaut, J., & Strasser, M. (2023). Application of micro-CT to resolve textural properties and assess primary sedimentary structures of deep-marine sandstones. *The Depositional Record*, *10*(5), 559–580. https://doi.org/10.1002/dep2.261

Daigle, H. (2014). Microporosity development in shallow marine sediments from the Nankai Trough. *Marine Geology*, *357*, 293–303. https://doi.org/10.1016/j.margeo.2014.09.041

Dorador, J., Rodríguez-Tovar, F. J., & Titschack, J. (2020). Exploring computed tomography in ichnological analysis of cores from modern marine sediments. *Scientific Reports*, *10*(1), 201. https://doi.org/10.1038/s41598-019-57028-z

Eakins, B. W., & Sharman, G. F. (2010). *Volumes of the world's oceans from ETOPO1*. NOAA National Geophysical Data Center.

Elkhoury, J. E., Shankar, R., & Ramakrishnan, T. S. (2019). Resolution and limitations of X-ray micro-CT with applications to sandstones and limestones. *Transport in Porous Media*, *129*(1), 413–425. https://doi.org/10.1007/s11242-019-01275-1

Favali, P., & Beranzoli, L. (2006). Seafloor observatory science: A review. *Annals of Geophysics*, *49*(2/3), 515–567. http://hdl.handle.net/2122/1059

Forsberg, C. F., & Locat, J. (2005). Mineralogical and microstructural development of sediments on the Mid-Norwegian margin. *Marine and Petroleum Geology*, *22*(1–2), 109–122. https://doi.org/10.1016/j.marpetgeo.2004.12.002

Fox, C. A., Abdulla, H. A., Burdige, D. J., Lewicki, J. P., & Komada, T. (2018). Composition of dissolved organic matter in pore water of Anoxic marine sediments analyzed by 1H nuclear magnetic resonance spectroscopy. *Frontiers in Marine Science*, *5*. https://doi.org/10.3389/fmars.2018.00172

Freeman, T. J., & Schüttenhelm, R. T. E. (1990). *A geotechnical investigation of a deep ocean site* (pp. 255–275). ASTM Special Technical Publication. https://doi.org/10.1520/STP17240S

Gatter, R., Bartzke, G., Madhusudhan, B. N., Sharif, A., Clare, M. A., Vardy, M., & Huhn, K. (2025). Micro-computed tomography analysis of marine sediment samples from two piston cores, GS10-163-02PC (offshore Norway) and 64PE391-04 (offshore UK) [Dataset]. *PANGAEA*. https://doi.org/10.1594/PANGAEA.979915

Gatter, R., Clare, M. A., Hunt, J. E., Watts, M., Madhusudhan, B. N., Talling, P. J., & Huhn, K. (2020). *A multi-disciplinary investigation of the AFEN Slide: The relationship between contourites and submarine landslides*. (Vol. 500, pp. 173–193). Geological Society, London, Special Publications. https://doi.org/10.1144/SP500-2019-184

Gatter, R., Clare, M. A., Kuhlmann, J., & Huhn, K. (2021). Characterization of weak layers, physical controls on their global distribution and their role in submarine landslide formation. *Earth-Science Reviews*, *223*, 103845. https://doi.org/10.1016/j.earscirev.2021.103845

Goldfinger, C., Nelson, C. H., Morey, A. E., Johnson, J. R., Patton, J., Karabanov, E., et al. (2012). Turbidite event history – Methods and implications for Holocene paleoseismicity of the Cascadia subduction zone. *U. S. Geological Survey Professional Paper*. 1661F. https://doi.org/10.3133/pp1661F

Guntoro, P. I., Ghorbani, Y., Koch, P.-H., & Rosenkranz, J. (2019). X-Ray microcomputed tomgraphy (μCT) for mineral characterization: A review of data analysis methods. *Minerals*, *9*(3), 183. https://doi.org/10.3390/min9030183

Hage, S., Hubert-Ferrari, A., Lamair, L., Avsar, U., El Ouahabi, M., Van Daele, M., et al. (2017). Flow dynamics at the origin of thin clayey sand lacustrine turbidites: Examples from Lake Hazar, Turkey. *Sedimentology*, *64*(7), 1929–1956. https://doi.org/10.1111/sed.12380

Hampel, U. (2022). 6 – X-ray computed tomography. In M. Wang (Ed.), *Woodhead publishing series in electronic and optical materials, industrial tomography (special edition)* (pp. 207–229). https://doi.org/10.1016/B978-0-12-823015-2.00029-7

Hassan, A. E., Cushman, J. H., & Delleur, J. W. (1998). Significance of porosity variability to transport in heterogeneous porous media. *Water Resources Research*, *34*(9), 2249–2259. https://doi.org/10.1029/98WR01470

Hattab, M., Hammad, T., Fleureau, J.-M., & Hicher, P.-Y. (2013). Behaviour of a sensitive marine sediment: Microstructural investigation. *Géotechnique*, *63*(1), 71–84. https://doi.org/10.1680/geot.10.P.104

Howarth, J. D., Orpin, A. R., Kaneko, Y., Strachan, L. J., Nodder, S. D., Mountjoy, J. J., et al. (2021). Calibrating the marine turbidite palaeoseismometer using the 2016 Kaikōura earthquake. *Nature Geoscience*, *14*(3), 161–167. https://doi.org/10.1038/s41561-021-00692-6

Johnson, M., Peakall, J., Fairweather, M., Barnes, M., Davison, S., Xiaodong, J., et al. (2019). Sediment microstructure and the establishment of gas migration pathways during bubble growth. *Environmental Science and Technology*, *53*(21), 12882–12892. https://doi.org/10.1021/acs.est.9b03034

Jutzeler, M., White, J. D. L., Talling, P. J., McCanta, M., Morgan, S., Le Friant, A., & Ishizuka, O. (2014). Coring disturbances in IODP piston cores with implications for offshore record of volcanic events and the Missoula megafloods. *Geochemistry, Geophysics, Geosystems*, *15*(9), 3572–3590. https://doi.org/10.1002/2014GC005447

Katz, B. J., & Arango, I. (2018). Organic porosity: A geochemist's view of the current state of understanding. *Organic Geochemistry*, *123*, 1–16. https://doi.org/10.1016/j.orggeochem.2018.05.015

Ketcham, R. A., & Carlson, W. D. (2001). Acquisition, optimization and interpretation of X-ray computed tomographic imagery: Applications to the geosciences. *Computers & Geosciences*, *27*(4), 381–400. https://doi.org/10.1016/S0098-3004(00)00116-3

Kim, G. Y., Yoon, H. J., Kim, J. W., Kim, D. C., Khim, B. K., & Kim, S. Y. (2007). The effects of microstructure on shear properties of shallow marine sediments. *Marine Georesources & Geotechnology*, *25*(1), 37–51. https://doi.org/10.1080/10641190601177564

Kneafsey, T. J., & Moridis, G. J. (2014). X-Ray computed tomography examination and comparison of gas hydrate dissociation in NGHP-01 expedition (India) and Mount Elbert (Alaska) sediment cores: Experimental observations and numerical modeling. *Marine and Petroleum Geology*, *58*(Part A), 526–539. https://doi.org/10.1016/j.marpetgeo.2014.06.016

Koltermann, C. E., & Gorelick, S. M. (1996). Heterogeneity in sedimentary deposits: A review of structure-imitating, process-imitating, and descriptive approaches. *Water Resources Research*, *32*(9), 2617–2658. https://doi.org/10.1029/96WR00025

Lee, C., Yun, T. S., Lee, J. S., Bahk, J. J., & Santamarina, J. C. (2011). Geotechnical characterization of marine sediments in the Ulleung Basin, East Sea. *Engineering Geology*, *114*(1–2), 151–158. https://doi.org/10.1016/j.enggeo.2010.10.014

Leon, A. Z., Huvenne, V. A. I., Benoist, N. M. A., Ferugson, M., Bett, B. J., & Wynn, R. B. (2020). Assessing the repeatability of automated seafloor classification algorithms, with application in marine protected area monitoring. *Remote Sensing*, *12*(10), 1572. https://doi.org/10.3390/rs12101572

L'Heureux, J.-S., Longva, O., Steiner, A., Hansen, L., Vardy, M. E., Vanneste, M., et al. (2012). Identification of weak layers and their role for the stability of slopes at Finneidfjord, northern Norway. In Y. Yamada, et al. (Eds.), *Submarine mass movements and their consequences, advances in natural and technological hazards Research* (Vol. 31, pp. 321–330). https://doi.org/10.1007/978-94-007-2162-3_29

Li, J., Hussaini, S. R., & Dvorkin, J. (2020). Permeability-porosity relations from single image of natural rock: Subsampling approach. *Journal of Petroleum Science and Engineering*, *194*, 107541. https://doi.org/10.1016/j.petrol.2020.107541

Longva, O., Janbu, N., Blikra, L. H., & Bøe, R. (2003). The 1996 Finneidfjord Slide; seafloor failure and Slide dynamics. In Locat, et al. (Eds.), *Submarine mass movements and their consequences, advances in natural and technological hazards Research* (Vol. 19, pp. 531–538). Springer. https://doi.org/10.1007/978-94-010-0093-2_58

Lowe, D. R. (1975). Water escape structures in coarse-grained sediments. *Sedimentology*, *22*(2), 157–204. https://doi.org/10.1111/j.1365-3091.1975.tb00290.x

Lu, B., & Li, G. (2003). Physical and mechanical characteristics of seabed sediment microstructure in the northern shelf of the South China Sea. *Marine Georesources & Geotechnology*, *21*(1), 1–13. https://doi.org/10.1080/10641190306710

Lv, Y., Li, X., Fan, C., & Su, Y. (2021). Effects of internal pores on the mechanical properties of marine calcareous sand particles. *Acta Geotechnica*, *16*(10), 3209–3228. https://doi.org/10.1007/s11440-021-01223-8

Maire, E., & Withers, P. J. (2014). Quantitative X-ray tomography. *International Materials Reviews*, *59*(1), 1–43. https://doi.org/10.1179/1743280413Y.0000000023

Maltman, A. (Ed.) (1994). *Geological deformation of sediments* (p. 362). Springer. Retrieved from https://link.springer.com/book/10.1007/978-94-011-0731-0

Maltman, A. J., & Bolton, A. (2003). *How sediments become mobilized*. (Vol. 216, pp. 9–20). Geological Society, London, Special Publications. https://doi.org/10.1144/GSL.SP.2003.216.01.02

Mayer, L., Jakobssen, M., Allen, G., Dorschel, B., Falconer, R., Ferrini, V., et al. (2018). The nippon foundation – GEBCO Seabed 2030 project: The quest to see the world's oceans completely mapped by 2030. *Geosciences*, *8*(2), 63. https://doi.org/10.3390/geosciences8020063

Mees, F., Swennen, R., Van Geet, M., & Jacobs, P. (2003). *Applications of X-ray computed tomography in the geosciences*. (Vol. 215, pp. 1–6). Geological Society, London, Special Publications. https://doi.org/10.1144/GSL.SP.2003.215.01.01

Mitra, S., Paris, R., Bernard, L., Abbal, R., Charrier, P., Falvard, S., et al. (2024). X-ray tomography applied to tsunami deposits: Optimized image processing and quantitative analysis of particle size, particle shape, and sedimentary fabric in 3D. *Marine Geology*, *470*, 107247. https://doi.org/10.1016/j.margeo.2024.107247

Moore, R. L., Patera, A., Bonnin, A., & Ménez, B. (2022). Grating-based X-ray computed tomography for improved contrast on a heterogeneous geomaterial. *Frontiers in Earth Sciences*, *10*, 878738. https://doi.org/10.3389/feart.2022.878738

Morgan, E. C., Vanneste, M., Lecomte, I., Baise, L. G., Longva, O., & McAdoo, B. (2012). Estimation of free gas saturation from seismic reflection surveys by the genetic algorithm inversion of a P-wave attenuation model. *Geophysics*, *77*(4), R175–R187. https://doi.org/10.1190/geo2011-0291.1

Orhan, K., & Büyüksungur, A. (2020). Fundamentals of micro-CT imaging. In K. Orhan (Ed.), *Micro-computed tomography (micro-CT) in medicine and engineering*. Springer. https://doi.org/10.1007/978-3-030-16641-0_3

Orsi, T. H., Edwards, C. M., & Anderson, A. L. (1994). X-ray computed tomography: A nondestructive method for quantitative analysis of sediment cores. *Journal of Sedimentary Research*, *64*(3), 690–693. https://doi.org/10.1306/d4267e74-2b26-11d7-8648000102c1865d

Paganin, D., Mayo, S. C., Gureyev, T. E., Miller, P. R., & Wilkins, S. W. (2002). Simultaneous phase and amplitude extraction from a single defocused image of a homogeneous object. *Journal of Microscopy*, *206*(1), 33–40. https://doi.org/10.1046/j.1365-2818.2002.01010.x

Phillips, D. H., & Lannutti, J. J. (1997). Measuring physical density with X-ray computed tomography. *NDT & E International*, *30*(6), 339–350. https://doi.org/10.1016/S0963-8695(97)00020-0

Randolph, M. F., Gaudin, C., Gourvenec, S. M., White, D. J., Boylan, N., & Cassidy, M. J. (2011). Recent advances in offshore geotechnics for deep water oil and gas developments. *Ocean Engineering*, *38*(7), 818–834. https://doi.org/10.1016/j.oceaneng.2010.10.021

Ransom, B., Bennett, R. H., Baerwald, R., Hulbert, M. H., & Burkett, P.-J. (1999). In situ conditions and interactions between microbes and minerals in fine-grained marine sediments: A TEM microfabric perspective. *American Mineralogist*, *84*(1–2), 183–192. https://doi.org/10.2138/am-1999-1-220

Riedel, M., Freudenthal, T., Bergenthal, M., Haeckel, M., Wallmann, K., Spangenberg, E., et al. (2020). Physical porperties and core-log seismic integration from drilling at the Danbube deep-sea fan, Black Sea. *Marine and Petroleum Geology*, *114*, 104192. https://doi.org/10.1016/j.marpetgeo.2019.104192

Robinson, A. H., Callow, B., Böttner, C., Yilo, N., Provenzano, G., Falcon-Suarez, I. H., et al. (2021). Multiscale characterisation of chimneys/pipes: Fluid escape structures within sedimentary basins. *International Journal of Greenhouse Gas Control*, *106*, 103245. https://doi.org/10.1016/j.ijggc.2020.103245

Rodríguez-Tovar, F. J., Dorador, J., Mena, A., & Hernández-Molina, F. J. (2018). Lateral variability of ichnofabrics in marine cores: Improving sedimentary basin analysis using Computed Tomography images and high-resolution digital treatment. *Marine Geology*, *397*, 72–78. https://doi.org/10.1016/j.margeo.2017.12.006

Rothwell, R. G., & Rack, F. R. (2006). *New techniques in sediment core analysis: An introduction*. (Vol. 267, pp. 1–29). Geological Society, London, Special Publications. https://doi.org/10.1144/GSL.SP.2006.267.01.01

Rudolph, T. B., Ruckelshaus, M., Swilling, M., Allison, E. H., Österblom, H., Gelcich, S., & Mbatha, P. (2020). A transition to sustainable ocean governance. *Nature Communications*, *11*(1), 3600. https://doi.org/10.1038/s41467-020-17410-2

Sammartini, M., Moernaut, J., Kopf, A., Stegmann, S., Fabbri, S. C., Anselmetti, F. S., & Strasser, M. (2021). Propagation of frontally confined subaqueous landslides: Insights from combining geophysical, sedimentological, and geotechnical analysis. *Sedimentary Geology*, *416*, 105877. https://doi.org/10.1016/j.sedgeo.2021.105877

Santos, C. F., Ehler, C. N., Agardy, T., Andrade, F., Orbach, M. K., & Crowder, L. B. (2019). Chapter 30 – Marine spatial planning. In *World seas: An environmental evaluation* (2nd ed., Vol. 3, pp. 571–592). Ecological Issues and Environmental Impacts. https://doi.org/10.1016/B978-0-12-805052-1.00033-4

Santos, I. R., Eyre, B. D., & Huettel, M. (2012). The driving forces of porewater and groundwater flow in permeable coastal sediments: A review. *Estuarine, Coastal and Shelf Science*, *98*, 1–15. https://doi.org/10.1016/j.ecss.2011.10.024

Sasov, A., Liu, X., & Salmon, P. (2008). Compensation of mechanical inaccuracies in micro-CT and nano-CT. *Proceedings of SPIE, 7078, Developments in X-Ray Tomography VI*, *7078*, 70781C. https://doi.org/10.1117/12.793212

Sauvin, G., Vardy, M., Klinkvort, R. T., Vanneste, M., Forsberg, C. F., & Kort, A. (2022). State-of-the-Art ground model development for offshore renewables – TWN case study. *European Association of Geoscientists & Engineers*, *2022*, 1–5. https://doi.org/10.3997/2214-4609.202221109

Sawyer, W. B., Ransom, B., & Bennett, R. H. (1997). Geotechnical property variability of continental margin sediments: High-resolution vertical and lateral data from the northern California slope. *Marine Georesources & Geotechnology*, *15*(3), 283–304. https://doi.org/10.1080/10641199709379948

Saxena, N., Hofmann, R., Alpak, F. O., Dieterich, J., Hunter, S., & Day-Stirrat, R. J. (2017). Effect of image segmentation & voxel size on micro-CT computed effective transport & elastic properties. *Marine and Petroleum Geology*, *86*, 972–990. https://doi.org/10.1016/j.marpetgeo.2017.07.004

Saxena, N., Hows, A., Hofmann, R., Alpak, F. O., Dietderich, J., Appel, M., et al. (2019). Rock properties from micro-CT images: Digital rock transforms for resolution, pore volume, and field of view. *Advances in Water Resources*, *134*, 103419. https://doi.org/10.1016/j.advwatres.2019.103419

Schindelin, J., Arganda-Carreras, I., Frise, E., Kaynig, V., Longair, M., Pietzsch, T., et al. (2012). Fiji: An open-source platform for biological-image analysis. *Nature Methods*, *9*(7), 676–682. https://doi.org/10.1038/nmeth.2019

Schlüter, S., Sheppard, A., Brown, K., & Wildenschuld, D. (2014). Image processing of multiphase images obtained via X-ray microtomography: A review. *Water Resources Research*, *50*(4), 3615–3639. https://doi.org/10.1002/2014WR015256

Sheng, G., Su, Y., Zhao, H., & Liu, J. (2020). A unified apparent porosity/permeability model of organic porous media: Coupling complex pore structure and multimigration mechanisms. *Advances in Geo-Energy Research*, *4*(2), 115–125. https://doi.org/10.26804/ager.2020.02.01

Sleutel, S., Cnudde, V., Masschaele, B., Vlassenbroek, J., Dierick, M., Van Hoorebeke, L., et al. (2008). Comparison of different nano- and micro-focus X-ray computed tomography set-ups for the visualization of the soil microstructure and soil organic matter. *Computers & Geosciences*, *34*(8), 931–938. https://doi.org/10.1016/j.cageo.2007.10.006

Steiner, A., L'Heureux, J.-S., Kopf, A., Vanneste, M., Longva, O., Lange, M., & Haflidason, H. (2012). An in-situ free-fall piezocone penetrometer for characterizing soft and sensitive clays at Finneidfjord (northern Norway). In Y. Yamada, et al. (Eds.), *Submarine mass movements and their consequences. Advances in natural and technological hazards Research* (Vol. 31, pp. 99–109). Springer. https://doi.org/10.1007/978-94-007-2162-3_9

St. Martin, K., & Hall-Arber, M. (2008). The missing layer: Geo-technologies, communities, and implications for marine spatial planning. *Marine Policy*, *32*(5), 779–786. https://doi.org/10.1016/j.marpol.2008.03.015

Tonai, S., Kubo, Y., Tsang, M.-Y., Bowden, S., Die, K., Hirose, T., et al. (2019). A new method for quality control of geological cores by X-ray computed tomography: Application in IODP expedition 370. *Frontiers in Earth Sciences*, *7*, 117. https://doi.org/10.3389/feart.2019.00117

Tretiak, I., & Smith, R. A. (2019). A parametric study of segmentation threshold for X-ray CT porosity characterisation in composite materials. *Composites Part A: Applied Science and Manufacturing*, *123*, 10–24. https://doi.org/10.1016/j.compositesa.2019.04.029

Uramoto, G. I., Morono, Y., Uematsu, K., & Inagaki, F. (2014). An improved sample preparation method for imaging microstructures of fine-grained marine sediment using microfocus X-ray computed tomography and scanning electron microscopy. *Limnology and Oceanography: Methods*, *12*(7), 469–483. https://doi.org/10.4319/lom.2014.12.469

Van Daele, M., Cnudde, V., Duyck, P., Pino, M., Urrutia, R., & De Batist, M. (2014). Multidirectional, synchronously-triggered seismo-turbidites and debrites revealed by X-ray computed tomography (CT). *Sedimentology*, *61*(4), 861–880. https://doi.org/10.1111/sed.12070

Van der Bilt, W. G. M., Cederstrøm, J. M., Støren, E. W. N., Berben, S. M. P., & Rutledal, S. (2021). Rapid tephra identification in geological archives with computed tomography: Experimental results and natural applications. *Frontiers in Earth Sciences*, *8*, 622386. https://doi.org/10.3389/feart.2020.622386

Vandorpe, T., Collart, T., Cnudde, V., Lebreiro, S., Hernández-Molina, F. J., Alonso, B., et al. (2019). Quantitative Characterization of contourite deposits using medical CT. *Marine Geology*, *417*, 106003. https://doi.org/10.1016/j.margeo.2019.106003

Vanneste, M., Forsberg, C. F., Kvalstad, T. J., L'Heureux, J.-S., Longva, O., Chand, S., et al. (2011). Assessing offshore geohazards: Site surveying, sampling, and comparison of shallow, submarine landslides in coastal and deepwater environments, northern Norway. *Report to NDP/SEABED, Nr. 20100135-1*, 1–66.

Vanneste, M., Longva, O., L'Heureux, J. S., Vardy, M. E., Morgan, E., Forsberg, C. F., et al. (2013). Finneidfjord, a field laboratory for integrated submarine slope stability assessments and characterization of landslide-prone sediments: A review. In *Offshore Technology Conference, OTC 13OTC-P-686-OTC, Huston, Texas, USA*.

Vanneste, M., Sultan, N., Garziglia, S., Forsberg, C. F., & L'Heureux, J.-S. (2014). Seafloor instabilities and sedimetn deformation processes: The need for integrated, multi-disciplinary investigations. *Marine Geology*, *352*, 183–214. https://doi.org/10.1016/j.margeo.2014.01.005

Vardy, M. (2022). Which geohazards are really hazards for marine infrastructure. In *Second international meeting for applied geosciences & energy* (pp. 3629–3633). SEG Technical Program Extended Abstracts. https://doi.org/10.1190/image2022-w6-02.1

Vardy, M. E., L'Heureux, J. S., Vanneste, M., Longva, O., Steiner, A., Forsberg, C. F., et al. (2012). Multidisciplinary investigation of a shallow near-shore landslide, Finneidfjord, Norway. *Near Surface Geophysics*, *10*(4), 267–277. https://doi.org/10.3997/1873-2012022

Varkouhi, S., Cartwright, J. A., & Tosca, N. J. (2020). Anomalous compaction due to silica diagenesis – Textural and mineralogical evidence from hemipelagic deep-sea sediments of the Japan Sea. *Marine Geology*, *426*, 10604. https://doi.org/10.1016/j.margeo.2020.106204

Volpi, V., Camerlenghi, A., Hillenbrand, C. D., Rebesco, M., & Ivaldi, R. (2003). Effects of biogenic silica on sediment compaction and slope stability on the Pacific margin of the Antarctic Peninsula. *Basin Research*, *15*(3), 339–363. https://doi.org/10.1046/j.1365-2117.2003.00210.x

Waite, W. F., Kneafsey, T. J., Winters, W. J., & Mason, D. H. (2008). Physical property changes in hydrate-bearing sediment due to depressurization and subsequent repressurization. *Journal of Geophysical Research*, *113*(B7), B07102. https://doi.org/10.1029/2007JB005351

Wang, Y., & Miller, J. D. (2020). Current developments and applications of micro-CT for the 3D analysis of multiphase mineral systems in geometallurgy. *Earth-Science Reviews*, *211*, 103406. https://doi.org/10.1016/j.earscirev.2020.103406

Weitkamp, T., Diaz, A., David, C., Pfeiffer, F., Stampanoni, M., Cloetens, P., & Ziegler, E. (2005). X-ray phase imaging with a grating interferometer. *Optics Express*, *13*(16), 6296–6304. https://doi.org/10.1364/OPEX.13.006296

Wetzel, A. (1990). Interrelationships between porosity and other geotechnical properties of slowly deposited, fine-grained marine surface sediments. *Marine Geology*, *92*(1–2), 105–113. https://doi.org/10.1016/0025-3227(90)90029-J

Wildenschild, D., & Sheppard, A. P. (2013). X-ray imaging and analysis techniques for quantifying pore-scale structure and processes in subsurface porous medium systems. *Advances in Water Resources*, *51*, 217–246. https://doi.org/10.1016/j.advwatres.2012.07.018

Wilson, C. A., Bulat, J., & Long, D. (2005). The afen Slide. *British Geological Survey Commissioned Report CR/05/003*.

Wilson, C. A., Long, D., & Bulat, J. (2004). The morphology, setting and processes of the Afen Slide. *Marine Geology*, *213*(1–4), 149–167. https://doi.org/10.1016/j.margeo.2004.10.005

Withers, P. J., Bouman, C., Carmignato, S., Cnudde, V., Grimaldi, D., Hagen, C. K., et al. (2021). X-ray computed tomography. *Nature Reviews Methods Primers*, *1*, 18. https://doi.org/10.1038/s43586-021-00015-4

Zhang, P., Lee, Y. I., & Zhang, J. (2019). A review of high-resolution X-ray computed tomography applied to petroleum geology and a case study. *Micron*, *124*, 102702. https://doi.org/10.1016/j.micron.2019.102702

Zwanenburg, E. A., Williams, M. A., & Warnett, J. M. (2021). Review of high-speed imaging with lab-based x-ray computed tomography. *Measurement Science and Technology*, *33*(1), 012003. https://doi.org/10.1088/1361-6501/ac354a